

First differential cross-sections measurement for ZZ production in association with two jets
in the four-leptons final state in ATLAS.

A Dissertation

Presented to

The Faculty of the Graduate School of Arts and Sciences
Brandeis University

Department of Physics

Professor Gabriella Sciolla, Advisor

In Partial Fulfillment
of the Requirements for the Degree
Doctor of Philosophy

by
Prajita Bhattacharai

May 2023

This dissertation, directed and approved by Prajita Bhattacharai's Committee, has been accepted and approved by the Faculty of Brandeis University in partial fulfillment of the requirements for the degree of:

DOCTOR OF PHILOSOPHY

Wendy Cadge, Dean
Graduate School of Arts and Sciences

Dissertation Committee:

Professor Gabriella Sciolla, Department of Physics, Brandeis University
Professor Aram Apyan, Department of Physics, Brandeis University
Dr. Alessandro Tricoli, Brookhaven National Laboratory

Copyright by
Prajita Bhattacharai

2023

ABSTRACT

First differential cross-sections measurement for ZZ production in association with two jets
in the four-leptons final state in ATLAS.

A dissertation presented to the Faculty of the
Graduate School of Arts and Sciences of Brandeis University
Waltham, Massachusetts

By Prajita Bhattacharai

Table of Contents

Acknowledgements	iv
Abstract	iv
List of Tables	viii
List of Figures	ix
List of Abbreviations	xiv
I Introduction	1
II Theory	2
1 The Standard Model	3
1.1 Symmetries	3
1.2 Particles and Fields	5
1.3 Theoretical Formulation of the Standard Model	7
2 Limitations of the Standard Model	18
3 Phenomenology of Proton-Proton Collisions	19
4 Electroweak Diboson Physics	23
III The Large Hadron Collider	27
5 ATLAS Detector	27
6 Physics Object Reconstruction	27
6.1 Electrons	27
6.2 Muons	27
6.3 Jets	27
7 Future Upgrades	27

IV Analysis Overview 28

8	Goals	28
9	Phase Space Definition	29
9.1	Fiducial Volume	29
9.2	Signal Region	31
10	Reconstruction Selection	32
10.1	Electrons	32
10.2	Muons	32
10.3	Jets	33
10.4	Overlap Removal	34
11	Event Selection	35
11.1	Method Overview	38
11.2	Binning for Unfolding	40
11.3	Method Validation	41
11.4	Bias and Optimization	44
12	Definition of Measured Observables	48

V Analysis Strategy 50

13	Background Estimation	50
13.1	Data Driven Estimate of Fake Background	50
14	Unfolding	73
14.1	Method Overview	73
14.2	Binning for Unfolding	76
14.3	Method Validation	76
14.4	Bias and Optimization	80
15	Uncertainties on the Measurement	83
15.1	Theoretical Uncertainties	83

15.2 Experimental Uncertainties	83
VI Results	84
16 Differential Cross-sections	84
17 Effective Field Theory ReInterpretation	84
VII Conclusion	85
VIII Outlook	86
18 Run-3	86
19 High Luminosity LHC	86
References	87
Appendices	89
A Personal Contribution	90
B Additional Study on Unfolding Bias	90

List of Tables

1	Properties of SM gauge bosons. [1]	6
2	Summary of different interactions of fermions under different gauge theory. The check mark suggests that the fermions interact via associated force.	6
3	Electroweak quantum numbers of the SM half-integer spin fermions (quarks and leptons) arranged in a left-handed $SU(2)$ doublet and right-handed $SU(2)$ singlet. The down-type left-handed quarks in $SU(2)_L$ quark doublets d' , s' & b' are linear combinations of d , s , b quarks [2].	7
4	Details of the kinematic pre-selection applied to the dressed baseline electrons, muons, and jets.	30
5	Details of the selections applied to form a quadruplet and a dijet selection in the fiducial volume.	30
6	Definition of the baseline and signal electrons.	33
7	Definition of the baseline and signal muons.	33
8	Definition of the baseline and signal jets.	34
9	Overlap removal used in the analysis. An object removed in one step does not enter into the subsequent step.	34
10	Details of event selection.	37
11	Binning for all unfolded observables in VBS-Enhanced and suppressed regions.	42
12	Binning for all unfolded observables in VBS-Enhanced and suppressed regions.	77

List of Figures

1	The seventeen fundamental particles of the SM include three generations of twelve fermions, four gauge bosons, and the scalar Higgs bosons. [3]	5
2	Parton distribution functions $xf_q(x, Q^2)$ for reference momentum transfer $Q_0^2 = 10 \text{ GeV}^2$ (left) and $Q_0^2 = 10^4 \text{ GeV}^2$ (right). The dependence of momentum fraction z carried by a parton is extracted in global PDF fits from experimental data [4].	20
3	Phenomenology of di-Z boson production in association with two jets in proton-proton collider	22
4	Typical diagrams of LO qq and gg induced QCD $\alpha_S^2 \alpha_{EWK}^4$ production of $ZZjj$	23
5	Typical diagrams for LO gg loop induced the QCD $\alpha_S^4 \alpha_{EWK}^4$ production of $ZZjj$	24
6	Feynman diagrams at LO for the EWK α_{EWK}^6 production of $ZZjj$	25
8	Event display of a candidate $pp \rightarrow ZZjj \rightarrow e^+e^-\mu^+\mu^-jj$ recorded by the ATLAS experiment in Run-2 2017 data-taking period. The invariant mass of the reconstructed four leptons is $m_{4\ell} = 605 \text{ GeV}$, and that of the reconstructed di-jet is $m_{jj} = 2228 \text{ GeV}$. The large rapidity separation between the two jet cones (light yellow) on the opposite sides of the ATLAS detector and centrally produced two Z bosons defines the characteristic feature of the EWK production of $ZZjj$ [5].	36
9	Unfolding inputs from SM MC as a function of m_{jj} . remake first plot with ATLAS Label and stability	40
10	MC technical closure test of the unfolding procedure for m_{jj} . The detector-level MC distribution (in blue) is unfolded with the nominal SM unfolding inputs and compared to the particle-level distribution (in red) from the same MC. A perfect closure between unfolded and particle level distribution is observed	43

11	Injection test with dimension-8 <i>FT0</i> EFT operator. remake plots with ATLAS Label	44
12	Unfolding validation using physics variation where parton-initiated QCD (left) or the EWK process cross-sections are varied.	45
13	A step-by-step overview of the data-driven closure test to get the unfolding bias. remake plots with ATLAS Label	46
14	Unfolding bias (left) and statistical uncertainty (right) with up to 4 unfolding iterations as a function of m_{jj} in VBS-Suppressed region.	47
15	Figure showing the decay angle $\theta_{\ell 1 \ell 2}^*$ ($\theta_{\ell 3 \ell 4}^*$) of the negative lepton in the primary (secondary) pair's rest frame. [6].	49
16	A schematic of the non-prompt lepton production from secondary interaction. Jet activities surround the non-prompt muon, and the muon track does not point to the hard scatter interaction point.	51
17	An overview of the fake background estimation.	52
18	Origins of leptons in the signal region in events with a quadruplet and a dijet. The lepton origin is classified by the IFF classifier tool. Only leptons that are part of the signal quadruplet are shown. remake plots with label and larger y-axis	54
19	Origins of non-prompt leptons in the signal region in events with a signal quadruplet and a dijet. The events are normalized to the number of non-prompt electrons (left) and non-prompt muons (right). remake plots w/wo ATLAS label	55
20	Fraction of non-prompt electrons and muons in the $Z + jets$ and $t\bar{t}$ control regions. remake plots w/wo ATLAS label	56
21	Sources of non-prompt electrons in background control regions. Fake composition is unique in these control regions. remake plots w/wo ATLAS label	57

22	Sources of non-prompt muons in $Z + jets$ (left) and $t\bar{t}$ (right) control regions. remake plots w/wo ATLAS label	57
23	Origins of non-prompt electrons (left) and muons (right) in the combined control region. remake plots w/wo ATLAS label	58
24	Additional baseline electrons as a function of p_T in control regions. remake plots w/wo ATLAS label	59
25	Additional baseline muons as a function of p_T in control regions. remake plots w/wo ATLAS label	60
26	Fake efficiency of fake electrons measured in the combined control region from data as a function of its p_T , η , and n_{jets} . remake plots w/wo ATLAS label and change color	63
27	Fake efficiency of fake muons measured in the combined control region from data as a function of its p_T , η , and n_{jets} . remake plots w/wo ATLAS label and change color	64
28	Fake efficiency of fake electrons measured in the combined control region from data as a function of its p_T , and η in two slices of n_{jets} ($n_{jet} = 0$ left) and ($n_{jet} > 0$ right). remake plots w/wo ATLAS label, change the color of text for second plot and y-label	65
29	Fake efficiency of fake muons measured in the combined control region from data as a function of its p_T , and η in two slices of n_{jets} ($n_{jets} = 0$ left) and ($n_{jet} > 0$ right). remake plots w/wo ATLAS label, change the color of text for second plot and y-label	66
30	Uncertainties on the fake efficiency of the fake electrons measured in the com- bined control region from data as a function of its p_T , η , and n_{jets} . remake plots w/wo ATLAS label	67

31	Uncertainties on the fake efficiency of the fake muons measured in the combined control region from data as a function of its p_T , η , and n_{jets} . remake plots w/wo ATLAS label	68
32	Sources of non-prompt electrons and muons in the different flavors and the same charge validation regions. remake plots with ATLAS Label	69
33	Yield as a function of $m_{4\ell}$ in the different flavor (top) and same charge (bottom) validation regions. In both regions, the MC prediction matches more closely with data when the fake background events are estimated using the data-driven fake-factor method. remake plots with ATLAS Label and cleaning other labels	70
34	Data and MC yield comparison for different flavor validation regions (left) and same charge validation region (right) as a function of several kinematic observables. remake plots with ATLAS Label and cleaning other labels	71
35	MC prediction and fake-factor method estimate of the fake background as a function of $m_{4\ell}$ (left) and $p_{T,4\ell}$ (right) in the VBS-Enhanced region. Black bands represent the systematic uncertainties from the fake factor method. remake plots with ATLAS Label and cleaning other labels	72
36	SM prediction and fake background estimated from the fake-factor method as a function of $m_{4\ell}$ (left) and $p_{T,4\ell}$ (right) in the VBS-Enhanced region. Black bands represent the systematic uncertainties from the fake factor method, which are negligible on the full signal region distribution. remake plots with ATLAS Label, cleaning other label and y-xis/ratio-axis title	72
37	Unfolding inputs from SM MC as a function of m_{jj} . remake first plot with ATLAS Label and stability	75

38	MC technical closure test of the unfolding procedure for m_{jj} . The detector-level MC distribution (in blue) is unfolded with the nominal SM unfolding inputs and compared to the particle-level distribution (in red) from the same MC. A perfect closure between unfolded and particle level distribution is observed	78
39	Injection test with dimension-8 <i>FT0</i> EFT operator. remake plots with ATLAS Label	79
40	Unfolding validation using physics variation where parton-initiated QCD (left) or the EWK process cross-sections are varied.	80
41	A step-by-step overview of the data driven closure test to get the unfolding bias. remake plots with ATLAS Label	81
42	Unfolding bias (left) and statistical uncertainty (right) with up to 4 unfolding iterations as a function of m_{jj} in VBS-Suppressed region.	82

- BSM: Beyond the Standard Model
- C: Charge conjugation
- CR: Control Region
- EFT: Effective Field Theory
- EWK: Electroweak
- FSR: Final State Radiation
- GRL: Good Run List
- H: Weak Hypercharge
- HF: Heavy Flavor
- I: Weak Isospin
- IFF: Isolation and Fake Forum
- $\mathcal{L}_{\mathcal{SM}}$: Lagrangian
- LB: Luminosity Block
- LF: Light Flavor
- LH: Left Handed
- MC: Monte Carlo
- P: Parity
- PDF: Parton Distribution Function
- Q: Electric Charge
- QGC: Quartic Gauge Coupling

- QED: Quantum Electrodynamics
- QCD: Quantum Chromodynamics
- (\mathcal{P}) : Poincare group
- RH: RightHanded
- SF-OC: Same-flavor, Opposite-charged
- SM: Standard Model
- SR: Signal Region
- T: Time-reversal
- TGC: Triple Gauge Coupling
- TTVA: Track-to-vertex association
- VBS: Vector Boson Scattering
- VR: Validation Region
- VRSC: Same Charge Validation Region
- VRDF: Different Flavor Validation Region
- VEV: Vacuum Expectation Value

Chapter I: Introduction

Chapter II: Theory

This chapter describes the theoretical framework of the experimental measurements discussed in this thesis. Section 1 introduces the Standard Model (SM) of particle physics and concepts relevant to the thesis. Section 2 discusses the outstanding problems with the Standard Model, thus, motivating the experimental measurement. Section 3 discusses the phenomenology of the proton-proton collisions, and Section 4 discusses the physics of two Z bosons production in an association of two jets.

1 The Standard Model

The SM of particle physics is a mathematical framework based on quantum field theory, which incorporates quantum mechanics and special relativity. The SM describes all known fundamental particles in nature and their interactions. It consists of two sets of particles with intrinsic angular momentum, half-integer-spin fermions that are fundamental constituents of matter particles, and force-carrying integer-spin bosons. The seventeen fundamental particles of the SM and their properties, such as mass, charge, and intrinsic spin, are shown schematically by figure 1. Two textbooks on particle physics, Mark Thomson’s Modern Particle Physics [7], and Halzen & Martin’s Quarks & Leptons [2] guide the discussion written in this section.

1.1 Symmetries

The fundamental particles of the SM and their interactions can be described by constructing a general renormalizable Lagrangian (\mathcal{L}_{SM}) that respects certain sets of given symmetries. The Lagrangian of the SM is independent of the reference frame, naturally respecting the complete external symmetries of special relativity, the Poincare group (\mathcal{P}). Thus, the SM is invariant under spacetime translations, boosts, and rotations. Additionally, by construct of the Lagrangian, the SM respects an internal local gauge symmetry $SU(3)_C \otimes SU(2)_L \otimes U(1)_Y$. The $SU(3)_C$ symmetry is associated with the Quantum Chromodynamics (QCD) discussed in detail in Section 1.3.3. The $SU(2)_L \otimes U(1)_Y$ gauge symmetry discussed in 1.3.4 is associated with the unified electroweak theory that combines Quantum Electrodynamics (QED) and the weak interactions.

According to Noether’s theorem, a quantity is conserved for each continuous transformation that leaves the Lagrangian invariant [8]. Several interesting physical quantum numbers are conserved as a consequence of the symmetries respected by the SM. The $SU(3)_C$ in QCD conserves color charge. Weak isospin (I) and weak hypercharge (Y) are the quantum

numbers associated with the $SU(2)_L$ and $U(1)_Y$ gauge groups, respectively. At low energies the $SU(2)_L \otimes U(1)_Y$ symmetry is spontaneously broken and will be discussed in Section 1.3.4. The $SU(2)_L$ group follows a chiral structure where the gauge fields couple explicitly to the left-handed (LH) chiral fermions states and the right-handed (RH) chiral anti-fermions states.

The SM also respects CPT symmetry, a combination of three additional discrete symmetries, charge conjugation (C), parity (P), and time-reversal (T). The charge-conjugation transformation transforms particles to anti-particles by reversing the quantum numbers, whereas the parity transformation transforms left-handed particles to right-handed particles.

1.2 Particles and Fields

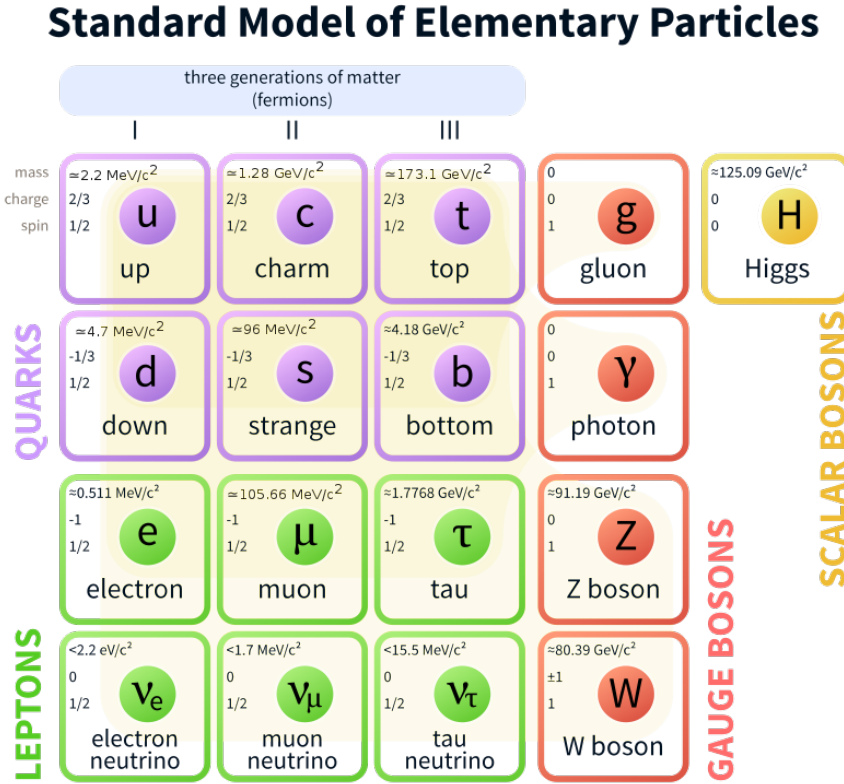


Figure 1: The seventeen fundamental particles of the SM include three generations of twelve fermions, four gauge bosons, and the scalar Higgs bosons. [3]

The twelve half-integer-spin fermions can be distinguished further into two categories, leptons and quarks, each having three generations of particles with similar properties as shown schematically by figure 1. For each fermion, there exists an anti-fermion with the same additive quantum numbers but with opposite signs. Four spin 1 bosons shown in Table 1 are collectively called the gauge bosons. Quanta of these gauge fields mediate the electromagnetic, weak, and strong interactions and are invariant under various local gauge transformations [9]. As summarized by Table 2, fermions take part in different interactions. A gauge coupling parameter governs the strength of the interaction.

Massless photon (γ) mediates the electromagnetic interaction, whereas the massive W

Table 1: Properties of SM gauge bosons. [1]

Interaction Type		Particle	Q	Mass [GeV]	Symmetry Group
Electroweak	Electromagnetic	Photon (γ)	0	0	$SU(2) \otimes U(1)$
	Weak	W^\pm	± 1	80.4	
		Z boson	0	91.2	
Strong		gluons (g)	0	0	$SU(3)$

Table 2: Summary of different interactions of fermions under different gauge theory. The check mark suggests that the fermions interact via associated force.

Particles		Strong $SU(3)$	Electromagnetic $U(1)$	Weak $SU(2)$
Quarks	u, c, t d, s, b	✓	✓	✓
Leptons	e, μ, τ ν_e, ν_μ, ν_τ	-	✓	✓

and Z bosons mediate weak interaction. The electric charge (Q), which is conserved in all interactions, is related to the isospin and hypercharge by $Q = I_3 + \frac{Y}{2}$, where I_3 is the third component of the weak isospin. As a consequence of the chiral structure of $SU(2)_L$, each generation of fermion contains a left-handed doublet with $I_3 = \pm \frac{1}{2}$ and a right-handed singlet carrying $I_3 = 0$ as shown in Table 3.

Each generation of lepton, electron (e), muon (μ) and tau (τ) is accompanied by a neutral particle called neutrino (ν) with same lepton flavor ($\nu_e, \nu_\mu \& \nu_\tau$). The SM neutrinos are their own anti-particles, and the theory only predicts the left-handed neutrinos. The SM conserves the lepton flavor in all interactions.

The quarks are categorized further into two categories, the up-type quarks with $+\frac{2}{3}$ charge and the down-type quarks with $-\frac{1}{3}$ charge. Up (u), charm (c), & top (t) are the first, second, and third generation of the up-type quarks, while the down (d), strange (s) & bottom (b) are the three generations of the down-type quarks. The quarks interact strongly with one another by strong interaction mediated by the massless neutral gluons, which follow from $SU(3)$ gauge symmetry by exchange of color charges. Each quark can have either one

Table 3: Electroweak quantum numbers of the SM half-integer spin fermions (quarks and leptons) arranged in a left-handed $SU(2)$ doublet and right-handed $SU(2)$ singlet. The down-type left-handed quarks in $SU(2)_L$ quark doublets d' , s' & b' are linear combinations of d , s , b quarks [2].

Particle Types	First	Second	Third	I_3	Y	Q
Leptons	$\begin{pmatrix} e \\ \nu_e \end{pmatrix}_L$	$\begin{pmatrix} \mu \\ \nu_\mu \end{pmatrix}_L$	$\begin{pmatrix} \tau \\ \nu_\tau \end{pmatrix}_L$	$-\frac{1}{2}$ $\frac{1}{2}$	-1 -1	-1 0
	e_R	μ_R	τ_R	0	-2	-1
Quarks	$\begin{pmatrix} u \\ d' \end{pmatrix}_L$	$\begin{pmatrix} c \\ s' \end{pmatrix}_L$	$\begin{pmatrix} t \\ b' \end{pmatrix}_L$	$\frac{1}{2}$ $-\frac{1}{2}$	$\frac{1}{3}$ $\frac{1}{3}$	$\frac{2}{3}$ $-\frac{1}{3}$
	u_R	c_R	t_R	0	$\frac{4}{3}$	$\frac{2}{3}$
	d_R	s_R	b_R	0	$-\frac{2}{3}$	$-\frac{1}{3}$

of the three color charges (red, blue &, green), whereas an anti-quark can have either an anti-red, anti-blue or anti-green color charge. There are eight gluons in the SM with color charges formed by a combination of either of the two color charges. Since gluons have a color charge, they interact with other gluons strongly. Only color-neutral hadronic states formed by a combination of quarks and gluons are observed experimentally.

Higgs boson is the only spin-0 scalar particle in the SM and has no charge. It gives masses to all other particles through Spontaneous Symmetry Breaking, which is discussed in Section 1.3.4.

1.3 Theoretical Formulation of the Standard Model

Relativistic quantum field theory is the theoretical framework of the SM that describes elementary particles and their interactions. This section introduces the framework.

1.3.1 Lagrangian of the Standard Model

The Lagrangian density given in equation 1.1 describes the dynamics of the SM and is invariant under the local gauge transformation of the $SU(3)_C \otimes SU(2)_L \otimes U(1)_Y$ symmetry group.

$$\mathcal{L}_{SM} = -\frac{1}{4}F_{\mu\nu}F^{\mu\nu} + i\bar{\psi}\gamma^\mu D_\mu\psi + |D_\mu\phi|^2 + -V(\phi) + \bar{\psi}_i y_{ij}\psi_j\phi + h.c. \quad (1.1)$$

The first term $-\frac{1}{4}F_{\mu\nu}F^{\mu\nu}$ describes the dynamics of the gauge boson interactions, the second term $i\bar{\psi}\gamma^\mu D_\mu\psi$ describes the interaction of the fermion fields. The third term $|D_\mu\phi|^2$ describes the couplings between the Higgs boson and gauge bosons, whereas the term $V(\phi)$ represents the Higgs potential and its self-interactions. The second last term $\bar{\psi}_i y_{ij}\psi_j\phi$ generates masses for fermions based on their Yukawa couplings y_{ij} to the Higgs field. Similarly, the last term $h.c.$ generates masses for anti-fermions.

1.3.2 Quantum Electrodynamics

Quantum electrodynamics describes electromagnetic interaction. The Lagrangian density (\mathcal{L}_{Dirac}) describes the free propagation of a fermion in a vacuum as:

$$\mathcal{L}_{Dirac} = \bar{\psi}i\gamma^\mu\partial_\mu\psi - m\bar{\psi}\psi \quad (1.2)$$

where ψ is the fermionic spinor, γ^μ represents the Dirac matrices with μ being the Lorentz index running from 0 to 3, ∂^μ is the covariant derivative and m is the mass of the fermion.

The Lagrangian in equation 1.2 is invariant under a $U(1)$ global gauge transformation,

$$\psi \rightarrow \psi' = e^{iq\alpha}\psi, \quad (1.3)$$

where q is a parameter of the transformation itself and α is a real phase factor. However, under the local gauge transformation of form

$$\psi \rightarrow \psi' = e^{iq\alpha(x)}\psi \quad (1.4)$$

where α depends on $x = (x_0, x_1, x_2, t)$ the Dirac Lagrangian in equation 1.2 is not invariant.

To make the Lagrangian of equation 1.2 invariant, a gauge field A_μ with the following transformation properties is introduced,

$$A_\mu \rightarrow A_\mu - \partial_\mu \alpha \quad (1.5)$$

A_μ couples to fermionic fields $\psi(x, t)$ with strength q . A covariant derivative specific to the local gauge transformation is defined as:

$$D_\mu = \partial_\mu - iqA_\mu \quad (1.6)$$

The quantity q can be interpreted as the electric charge $-e$ of fermion, which gives the coupling strength of QED. With these substitutions, the Dirac Lagrangian in equation 1.2 changes to the following

$$\mathcal{L} = \bar{\psi}(i\gamma^\mu D_\mu - m)\psi \quad (1.7)$$

which is invariant under $U(1)$ gauge transformation respecting the $U(1)$ gauge symmetry.

The gauge field A_μ can be interpreted as the photon field and is related to the electromagnetic field tensor by

$$F_{\mu\nu} = \partial_\mu A_\nu - \partial_\nu A_\mu \quad (1.8)$$

The gauge invariant kinetic term of photon $-\frac{1}{4}F_{\mu\nu}F^{\mu\nu}$ can be inserted into the Lagrangian in equation 1.7 which gives us the full Lagrangian of QED invariant under $U(1)$ gauge transformation.

$$\mathcal{L}_{QED} = -\frac{1}{4}F_{\mu\nu}F^{\mu\nu} + \bar{\psi}(i\gamma^\mu D_\mu - m)\psi \quad (1.9)$$

\mathcal{L}_{QED} in equation 1.9 is the full Lagrangian for QED, and the electromagnetic phenomena can be derived by solving for the equations of motion applying the Lorentz gauge condition $\partial_\mu A^\mu = 0$.

1.3.3 Quantum Chromodynamics

Quantum Chromodynamics defines the interaction between the quarks, requiring $SU(3)$ gauge transformation on the quark field with color charge j (red, blue, or green).

The Dirac Lagrangian for a quark can be modified to include all possible colors of quark field q_j as

$$\mathcal{L} = \bar{q}_j(i\gamma^\mu \partial_\mu - m)q_j \quad (1.10)$$

The generators of the $SU(3)$ group are eight linearly independent traceless Gell-Mann matrices that do not commute with each other such that

$$[T_a, T_b] = if_{abc}T_c \quad (1.11)$$

where f_{abc} is the structure constant of $SU(3)$

The local $SU(3)$ gauge transformation is

$$q(x) \rightarrow e^{i\alpha_a(x)T_a}q(x) \quad (1.12)$$

where $T_a = \frac{\lambda_a}{2}$, and $a = 1, 2 \dots 8$. To understand the source of gauge invariance in the Lagrangian in equation , we can consider an infinitesimal transformation of the color field as

$$q(x) \rightarrow [1 + i\alpha_a(x)T_a]q(x) \ni \partial_\mu q \rightarrow (1 + i\alpha_a T_a)\partial_\mu q + iT_a q \partial_\mu \alpha_a \quad (1.13)$$

The last term $iT_a q \partial_\mu \alpha_a$ breaks the gauge invariance. Similar to QED, eight gauge fields corresponding to each $a = 1, 2 \dots 8$ G_μ^a with following transformation properties are introduced

$$G_\mu^a \rightarrow G_\mu^a - \frac{1}{g_s} \partial_\mu \alpha_a - f_{abc} \alpha_b G_\mu^c \quad (1.14)$$

These gauge fields G_μ^a are the gluon fields. Similar to QED, the covariant derivative is defined as

$$D_\mu = \partial_\mu + ig_s \frac{\lambda_a}{2} G_\mu^a \quad (1.15)$$

where g_s is the coupling strength of the gluon fields to the quark fields.

The Lagrangian density in equation 1.10 is then

$$\mathcal{L} = \bar{q}_j (i\gamma^\mu D_\mu - m) q_j \quad (1.16)$$

Similar to QED, a gauge-invariant kinetic term $-\frac{1}{4} G_{\mu\nu}^a G_a^{\mu\nu}$, dependent on the field strength tensor $G_{\mu\nu}^a$ is added to equation 1.16 to give the full QCD Lagrangian. The kinetic terms allow self-interaction within the gluon fields, which is an important feature of QCD. $G_{\mu\nu}^a$ is the field strength tensor defined as

$$G_{\mu\nu}^a = \partial_\mu G_\nu^a - \partial_\nu G_\mu^a - g_s f_{abc} G_\mu^b G_\nu^c \quad (1.17)$$

Therefore, the complete $SU(3)$ gauge invariant Lagrangian describing the quarks and gluons interaction is

$$\mathcal{L}_{QCD} = \bar{q}_j (i\gamma^\mu D_\mu - m) q_j - \frac{1}{4} G_{\mu\nu}^a G_a^{\mu\nu} \quad (1.18)$$

1.3.4 Electroweak Theory

Weak interactions describe the interactions mediated by massive gauge bosons. Fermi formulated the weak interaction in 1934 to explain the beta decay using four fermion interaction vertex. The formulation successfully describes the beta decay at low energies when the in-

teraction energy is much smaller than the W boson mass. A unified electroweak theory was formulated by Glashow in 1961 [10] by extending the $SU(2)$ symmetric non-Abelian gauge theory developed by Yang and Mills in 1954 [11] to $SU(2) \otimes U(1)$ gauge theory. Above the unification threshold, the differences in the electromagnetic and weak interactions are not apparent.

Experimental observations suggest weak interactions violate parity by only affecting the left-handed fermion and right-handed anti-fermion fields. Thus the unified electroweak theory are described by $SU(2)_L \otimes U(1)_Y$ gauge interactions. Similar to the electric charge Q conserved in QED by $U(1)$ symmetry, the weak hypercharge ($Y = 2(Q - I_3)$) related to the electric charge and the weak isospin I_3) is conserved by the $U(1)_Y$ symmetry. The fermion fields are represented by the left-handed doublets χ_L and the right-handed singlets ψ_R , introduced in table 3. The doublet and singlet field for the first generation of leptons and quarks are,

$$\chi_L = \begin{pmatrix} \nu_e \\ e \end{pmatrix}_L \quad \& \quad \chi_L = \begin{pmatrix} u \\ d \end{pmatrix}_L$$

$$\psi_R = e_R \quad \& \quad \psi_R = u_R \& d_R$$

The Lagrangian for these fermion fields should be invariant under local gauge transformation corresponding to both $SU(2)_L$ and $U(1)_Y$ symmetry as,

$$\chi_L \rightarrow e^{i\beta(x)Y + i\alpha_a(x)\tau_a} \chi_L \tag{1.19}$$

$$\psi_R \rightarrow e^{i\beta(x)Y} \psi_R \tag{1.20}$$

where, $\beta(x)$ and $\alpha(x)$ are the local phase transformation for $U(1)_Y$ and $SU(2)_L$ symmetry groups respectively. Weak hypercharge operator Y and Pauli matrices $\tau_{a=1,2,3}$ are generators of $U(1)_Y$ and $SU(2)_L$ symmetry groups respectively. Similar to the formulation in QED and QCD discussed in Section 1.3.2 and 1.3.3, four new field strength tensors $B_{\mu\nu}$ and $W_{\mu\nu}^a$

corresponding to respectively the $U(1)_Y$ and $SU(2)_L$ transformations are introduced. The $SU(2)_L \otimes U(1)_Y$ gauge-invariant Lagrangian for a massless fermion and massless gauge fields is:

$$\mathcal{L}_0 = \bar{\chi}_L \gamma^\mu [i\partial_\mu - g \frac{\tau_a}{2} W_\mu^a + \frac{g'}{2} B_\mu] \chi_L + \bar{\psi}_R \gamma^\mu [i\partial_\mu + g' B_\mu] \psi_R - \frac{1}{4} W_{\mu\nu}^a W_a^{\mu\nu} - \frac{1}{4} B_{\mu\nu} B^{\mu\nu} \quad (1.21)$$

where similar to QED and QCD, field strength tensors are defined in terms of the covariant derivative to preserve gauge-invariance in kinetic terms as,

$$B_{\mu\nu} = \partial_\mu B_\nu - \partial_\nu B_\mu \quad (1.22)$$

$$W_{\mu\nu}^a = \partial_\mu W_\nu^a - \partial_\nu W_\mu^a + g \epsilon^{abc} W_\mu^b W_\nu^c \quad (1.23)$$

The non-Abelian part of the $SU(2)_L$ transformation is represented by the last term of equation 1.23, which gives the quartic and triple self-interactions between the gauge bosons with coupling strength g .

The electroweak Lagrangian in equation 1.21 contains two terms, one of which gives rise to the charged-current interaction with the two $SU(2)$ boson field

$$W_\mu^\pm = \frac{W_\mu^1 \mp i W_\mu^2}{\sqrt{2}} \quad (1.24)$$

via exchange of the W^\pm bosons and the neutral current interactions from the two neutral gauge boson fields W_μ^3 and B_μ .

The Lagrangian for the charged-current interaction for the first generation of quarks and leptons is,

$$\mathcal{L}_{CC} = \frac{g}{2\sqrt{2}} \{ W_\mu^\dagger [\bar{u} \gamma^\mu (1 - \gamma_5) d + \bar{\nu}_e \gamma^\mu (1 - \gamma_5) e] + h.c. \} \quad (1.25)$$

The $SU(2)_L$ charged-current interaction Lagrangian for the next two generations follows the same, establishing the universality of the quark and lepton interactions as a direct

consequence of the gauge symmetry.

The neutral-current Lagrangian is given by,

$$\mathcal{L}_{NC} = \sum_j \bar{\psi}_j \gamma^\mu \{ A_\mu [g \frac{\tau_3}{2} \sin\theta_W + g' Y \cos\theta_W] + Z_\mu [\frac{\tau_3}{2} \cos\theta_W - g' Y \sin\theta_W] \} \psi_j \quad (1.26)$$

where the two neutral gauge fields Z_μ and A_μ associated with Z boson and photon governing the weak neutral and electromagnetic interactions are obtained from an arbitrary linear combination of the W_μ^3 and B_μ fields as

$$\begin{pmatrix} A_\mu \\ Z_\mu \end{pmatrix} = \begin{pmatrix} \cos\theta_W & \sin\theta_W \\ -\sin\theta_W & \cos\theta_W \end{pmatrix} \begin{pmatrix} B_\mu \\ W_\mu^3 \end{pmatrix} \quad (1.27)$$

The following condition is imposed to obtain QED from A_μ :

$$g \sin\theta_W = g' \cos\theta_W = e \quad \& \quad Y = Q - T_3 \quad (1.28)$$

where $T_3 = \frac{\tau_3}{2}$ is the weak isospin and θ_W is the Weinberg mixing angle, which can be measured experimentally and expressed in terms of the two $SU(2)_L$ coupling g' and $U(1)_Y$ coupling g as:

$$\sin\theta_W = \frac{g'}{\sqrt{g^2 + g'^2}} \quad \& \quad \cos\theta_W = \frac{g}{\sqrt{g^2 + g'^2}} \quad (1.29)$$

The Lagrangian in equation 1.21 describes the electroweak interactions only for massless fermions and massless gauge bosons, which contradicts the experimental observations. The mass origin of the fermions and gauge bosons is discussed in Section 1.3.5 below.

1.3.5 Higgs Mechanism

Massive gauge bosons in the Lagrangian 1.21 can be accommodated through the Brout-Englert-Higgs (BEH) mechanism by introducing a complex scalar field ϕ in the spinor rep-

resentation of $SU(2)_L$ doublet as [12],

$$\phi = \begin{pmatrix} \phi^+ \\ \phi^0 \end{pmatrix} \quad (1.30)$$

A new term in the SM Lagrangian \mathcal{L}_{BEH} depending on this scalar field can be defined as,

$$\mathcal{L}_{BEH} = (D_\mu \phi)^\dagger (D^\mu \phi) - \mu^2 \phi^\dagger \phi + \lambda(\phi^\dagger \phi)^2 \quad (1.31)$$

The first term $(D_\mu \phi)^\dagger (D^\mu \phi)$ describes the kinematic of the new fields, and the BEH potential $V(\phi)$ is given by the second term as,

$$V(\phi) = \lambda(\phi^\dagger \phi)^2 - \mu^2 \phi^\dagger \phi \quad (1.32)$$

The term $\lambda(\phi^\dagger \phi)^2$ describes the quartic self-interactions of the scalar fields, and the vacuum stability imposes $\lambda > 0$.

For $\mu^2 > 0$, the scalar field develops a nonzero Vacuum Expectation Value (VEV) which spontaneously breaks the symmetry. Due to the symmetry of $V(\phi)$ an infinite number of degenerate states exists with the potential v only depending on the combination of $\phi^\dagger \phi$ [13] with minimum energy satisfying $\phi^\dagger \phi = \frac{v^2}{2}$. This minimum energy requirement reduces one of the four degrees of freedom of the complex scalar field ϕ . A gauge transformation can eliminate the three remaining degrees of freedom. We can choose ϕ by eliminating the upper component and the imaginary part of the lower component of the complex scalar field as,

$$\langle \phi \rangle = \frac{1}{\sqrt{2}} \begin{pmatrix} 0 \\ v + H(x) \end{pmatrix} \quad ; \quad H(x) = H^*(x) \frac{1}{\sqrt{2}} \begin{pmatrix} 0 \\ v \end{pmatrix} \quad (1.33)$$

where the Higgs field (H) emerges as the excitation from the vacuum state, this choice of the minimum spontaneously breaks the gauge symmetry [14].

After substituting the ϕ in the Lagrangian in equation 1.31, the kinetic term takes the form

$$\begin{aligned} \mathcal{L}_{BEH\ Kinetic} &= \frac{\lambda}{2}v^4 \\ &+ \frac{1}{2}\partial_\mu H\partial^\mu H - \lambda v^2 H^2 + \frac{\lambda}{\sqrt{2}}vH^3 + \frac{\lambda}{8}H^4 \\ &+ \frac{1}{4}(v + \frac{1}{\sqrt{2}}H)^2(W_\mu^1 \quad W_\mu^2 \quad W_\mu^3 \quad B_\mu) \begin{pmatrix} g^2 & 0 & 0 & 0 \\ 0 & g^2 & 0 & 0 \\ 0 & 0 & g^2 & gg' \\ 0 & 0 & gg' & g^2 \end{pmatrix} \begin{pmatrix} W^{1\mu} \\ W^{2\mu} \\ W^{3\mu} \\ B^\mu \end{pmatrix} \end{aligned} \quad (1.34)$$

where the first line is the vacuum energy density and can be ignored in the case of QFT. The second line describes the triple and quartic self-interactions of the Higgs field as well as the mass term of the real scalar field H as $m_H = 2\lambda v^2$. The last line contains the mass term for the vector bosons.

From equations 1.34 and 1.24 is evident the mass of the two charged vector bosons W^\pm is $m_W = \frac{1}{2}g^2v^2$. Similarly, from equations 1.34 and 1.27, mass of the Z boson is $m_Z = \frac{1}{2}(g^2 + g')v^2$ and mass of the photon is $m_\gamma = 0$.

The initial $SU(2)_L$ Lagrangian in equation 1.31 started with four gauge symmetries, which is reduced to a single $U(1)_Q$ gauge symmetry associated with the massless vector field in equation 1.34. This phenomenon in the Higgs mechanism is called the Electroweak Symmetry Breaking (EWSB) mechanism. As discussed above, the EWSB mechanism is at the heart of the SM by which the gauge boson gets the mass which also gives rise to the longitudinal polarization of the massive vector bosons. This thesis summarizes a measurement with an experimental sensitivity to such important property of the theory.

The last remaining piece in the SM is adding the fermion mass to the Lagrangian. A

simple Lagrangian with the fermion mass can be written as,

$$\mathcal{L}_{mass\ fermion} = -m(\bar{\chi}_L \psi_R + \bar{\psi}_R \chi_L) \quad (1.35)$$

This term violates $SU(2)_L$ gauge symmetry because the left-handed fermions are doublets, and the right-handed are singlets. Adding a scalar complex field $\phi = \frac{1}{\sqrt{2}} \begin{pmatrix} 0 \\ v + H(x) \end{pmatrix}$ in the Lagrangian becomes,

$$\mathcal{L}_{Yukawa, \ell} = \frac{G_\ell v}{\sqrt{2}} (\bar{\chi}_L \psi_R + \bar{\psi}_R \chi_L) - \frac{G_\ell}{\sqrt{2}} (\bar{\chi}_L \psi_R + \bar{\psi}_R \chi_L) H \quad (1.36)$$

with arbitrary parameters $G_{\ell=e,\mu,\tau}$. The constant in the first term $\frac{G_\ell v}{\sqrt{2}}$ represents the mass of the fermions, whereas the second term gives the interaction of fermions with the Higgs field.

Similarly, the mass terms for quarks follow but including the down-type quarks, the parameters corresponding to G_ℓ are matrices G_q^{ij} for the quark families i, j and up-type and down-type quarks as:

$$\mathcal{L}_{Yukawa, Q} = -G_d^{ij} (\bar{u}_i, \bar{d}_i)_L \phi d_{jR} - G_u^{ij} (\bar{u}_i, \bar{d}_i)_L \phi u_{jR} + h.c. \quad (1.37)$$

The final Standard Model Lagrangian is the sum of the QED (equation 1.9), QCD (equation 1.16), Boson self-interactions (equation 1.21), Higgs potential and self-interactions (equation 1.31), and the Higgs-fermion Yukawa coupling (equations 1.36 & 1.37), which in a compact form is written as equation 1.1.

2 Limitations of the Standard Model

Many discoveries have experimentally validated the Standard Model's predictions since the 20th century. The breakthrough discovery of the Higgs boson in 2012 at the LHC validated the last piece of the theory [15]& [16]. Many predicted parameters, such as production cross-sections and decay branching ratios for several processes, have been measured with high precision. No, statistically significant discrepancy from theory has been observed except for the W^\pm boson mass measurement from the CDF *II* Collaboration [17].

Despite the incredible success of the theory, experimental evidence suggests that the theory is incomplete. SM has the following limitations:

- SM fails to explain the gravitational force.
- SM only describes 5% of the universe. It fails to explain dark matter whose existence is experimentally supported by astrophysical observations such as galactic rotation curves and gravitational lensing [18]. It also does not explain dark energy.
- The CP violation allowed in SM cannot explain the amount of anti-matter asymmetry observed in the universe.
- The strengths of the four fundamental forces are different by many orders of magnitude. It has yet to be understood the hierarchy of such interactions.

These limitations suggest that the SM is an effective field theory, only describing an approximation of our universe, thus, motivating the experimental searches for new physics beyond the Standard Model (BSM). Experimentally there are two ways to look for BSM physics, direct searches, and indirect precision measurements. BSM-predicted particles are searched directly by direct searches. The thesis focuses on the indirect approach, where precisely measured SM-predicted differential cross-sections are compared with state-of-the-art theoretical predictions looking for hints of deviation caused by the BSM physics.

3 Phenomenology of Proton-Proton Collisions

The main results discussed in this thesis are differential cross-sections for di-Z boson production in association with two jets in a proton-proton collider at the center of mass energy of $\sqrt{s} = 13 \text{ TeV}$. Protons are composite particles made up of quarks and gluons. Thus, the theoretical formalism discussed above does not provide all the necessary tools for experimental cross-section measurements in hadron colliders. The differential cross-section $d\sigma$ for two particles is given by,

$$d\sigma = \frac{|\mathcal{M}|^2}{F} dQ \quad (3.1)$$

where F is the incident flux, and dQ represents the Lorentz invariant phase space factor. The scattering amplitude \mathcal{M} is the matrix element calculated from the Lagrangian density of the SM using a perturbative expansion [19].

The cross-section of a process with two initial-state partons p_1 and p_2 producing the final state X is given by:

$$d\sigma_{p_1 p_2 \rightarrow X} = \int dx_1 dx_2 \sum_{q_1, q_2} f_{q_1}(x_1, \mu_F) f_{q_2}(x_2, \mu_F) d\sigma_{q_1 q_2 \rightarrow X}(x_1, x_2, \mu_F, \mu_R) \quad (3.2)$$

where, q_1 , q_2 are the partons of the protons, and $d\sigma_{q_1 q_2 \rightarrow X}(x_1, x_2, \mu_F, \mu_R)$ is the partonic cross-section. The functions $f_{q_1}(x_1, \mu_F)$ & $f_{q_2}(x_2, \mu_F)$ are the parton distribution functions (PDF) representing the density of the partons q inside a proton carrying the longitudinal momentum fraction x . The PDFs are determined experimentally using data from deep-inelastic-scattering, jets production, and Drell Yan events [20] [21]. As shown by figure 2, a PDF of a parton depends on the reference value of the momentum transfer Q_0^2 . The differences are driven by modifications of partons' momenta resulting from the emission of gluons off of quarks and the splitting of gluons to $q\bar{q}$ pairs. A PDF at any value of Q^2 can be calculated using the PDF at reference scale Q_0^2 . The factorization scale μ_F determines

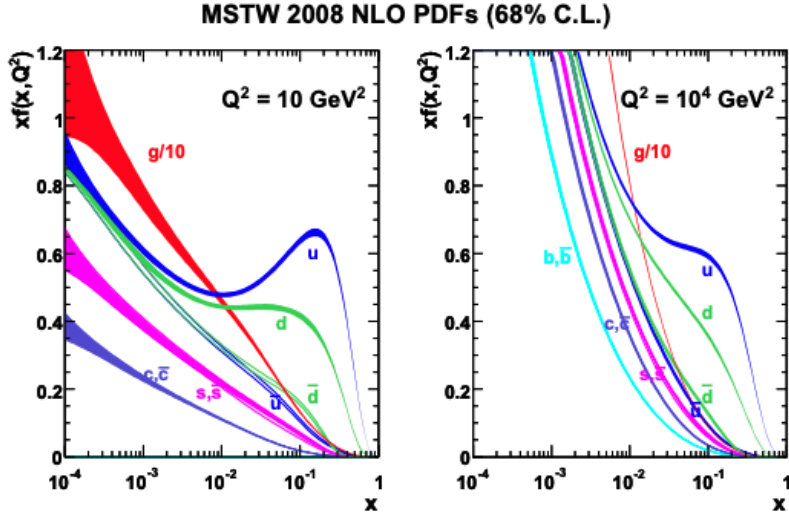


Figure 2: Parton distribution functions $xf_q(x, Q^2)$ for reference momentum transfer $Q_0^2 = 10 \text{ GeV}^2$ (left) and $Q_0^2 = 10^4 \text{ GeV}^2$ (right). The dependence of momentum fraction x carried by a parton is extracted in global PDF fits from experimental data [4].

the threshold whether the perturbative corrections modify the PDF or are included in the partonic cross-sections $d\sigma_{q_1 q_2}$ [19].

The partonic cross-section is calculated perturbatively as an expansion in terms of the strong coupling constant α_S as,

$$d\sigma_{q_1 q_2 \rightarrow X} = \alpha_S^k \sum_{m=0}^n c_m \alpha_S^m \quad (3.3)$$

The coefficient c_m depends on the center-of-mass energy, and theoretical calculations usually contain a finite number of coefficients. Leading order (LO) calculations include one term ($n = 0$), whereas next-to-leading order (NLO) and next-to-next-to-leading order (NNLO) contains two ($n = 1$) and three ($n = 2$) terms, respectively. The theoretical calculations relevant to the thesis are generally calculated at NLO. The higher-order terms in the series contain additional virtual loop contributions and real emissions of quarks and gluons. The presence of virtual loops beyond the LO introduces singularities in the calculation of scattering amplitudes. The divergences are controlled via the renormalization procedure, where

the singularities are absorbed by reparametrization of coupling and mass parameters. The renormalization process is energy-dependent. Therefore, the predicted cross-sections from theoretical calculations depend on the renormalization scale μ_R and the factorization scale μ_F . The scale dependence is varied in Monte Carlo simulations to derive uncertainties on the predicted cross-section due to missing higher-order contributions.

The additional partons of the two protons that interact in the hard interaction process lead to minor energy deposits in the detector, referred to as an underlying event. Any outgoing partons from the interaction emit multiple QCD radiation via the parton showering process, where the energy of each parton is split among an increasing number of other elementary particles. Due to the color confinement nature of QCD, at lower energies of the order of the pole of the QCD running coupling (λ_{QCD}), the partons are bound into stable and unstable hadrons. This process is named *hadronization* and leads to the formation of collimated sprays of charged and neutral hadrons in the detector called *jets*. Figure 3 schematically shows the phenomenology of di-Z boson production in association with two jets in the proton-proton collider. The theoretical predictions of such events are calculated using Monte Carlo (MC) simulations which include matrix element calculations for two partons giving two Z bosons, the parton showering, the effect of the underlying events, hadronizations, and pile-up. A comprehensive overview of the methods used in MC simulation is discussed in Ref [22].

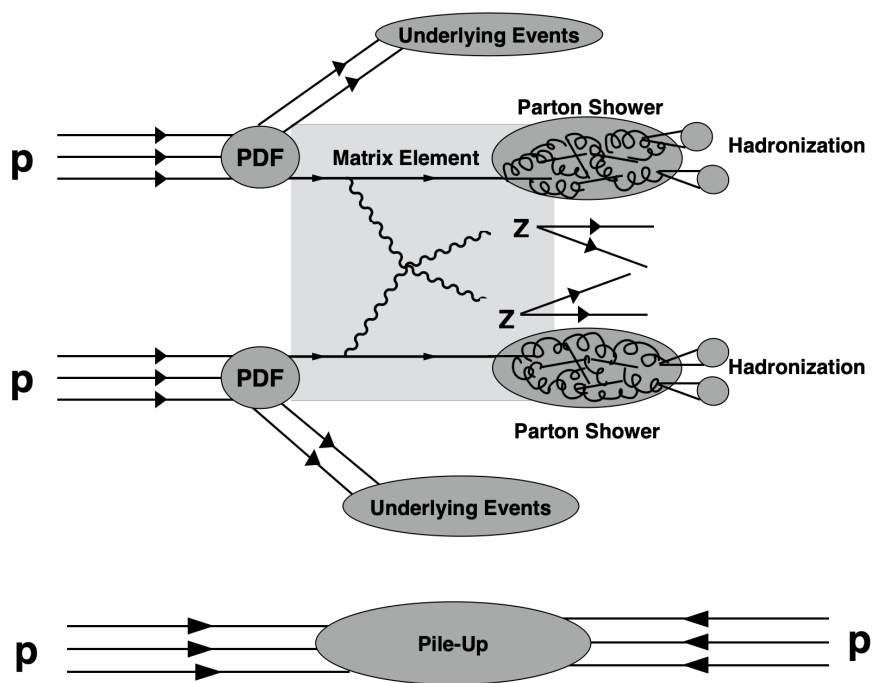


Figure 3: Phenomenology of di- Z boson production in association with two jets in proton-proton collider

4 Electroweak Diboson Physics

In LHC, two types of physics processes, the QCD production at the order $\alpha_S^{>2}\alpha_{EWK}^4$ and the EWK production at order α_{EWK}^6 contribute to the production of di- Z bosons in an association of two jets ($ZZjj$) [23]. Figures 4 and 5 show the Feynman diagram at leading order for the QCD $ZZjj$ process, whereas figure 6 shows the Feynman diagram at leading order for the EWK production of $ZZjj$ [24]. The EWK production consists of two sets of interactions, first, the Vector Boson Scattering processes involving either triple (figure 6a) or quartic (figure 6b) self-interactions of the gauge-bosons, and second the diagrams featuring the Higgs bosons (figure 6c & 6d). The scattering amplitudes of the VBS processes involving longitudinally polarized vector bosons grow quadratically with the center of mass energy (\sqrt{s}), eventually violating the unitarity bounds. The precise SM interference between the Higgs-featured process and the VBS process restores the unitarity [25]. As discussed in Section 1.3.5, the massive W and Z bosons get their masses via the BEH mechanism through EWSB. As a consequence of EWSB, the W and Z bosons acquire an additional degree of freedom (the longitudinal polarization mode) whose scattering interfere with the Higgs-featured processes. Thus, the study of electroweak production of the di- Z bosons in association with two jets provides a direct probe of the EWSB, which is at the heart of the SM [23].

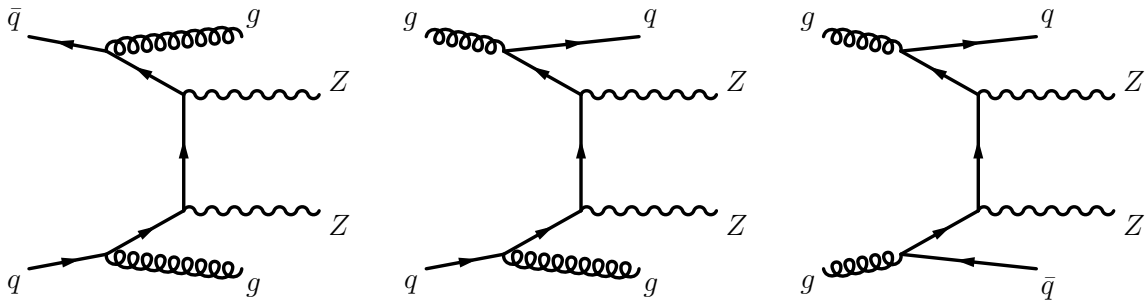


Figure 4: Typical diagrams of LO qq and gg induced QCD $\alpha_S^2\alpha_{EWK}^4$ production of $ZZjj$.

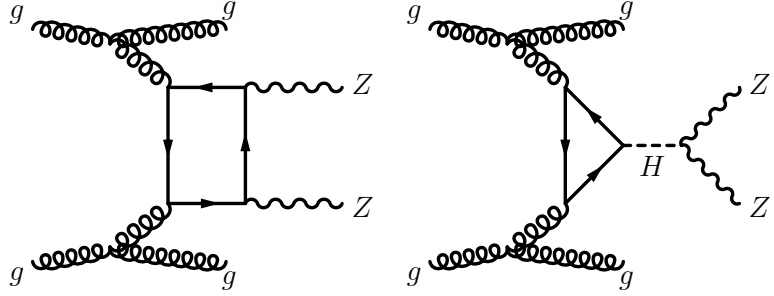


Figure 5: Typical diagrams for LO gg loop induced the QCD $\alpha_S^4 \alpha_{EWK}^4$ production of $ZZjj$.

The triple and quartic self-interactions of the gauge bosons arise from the square of the non-Abelian structure of $SU(2)$ in the kinetic term $\frac{1}{4}W_{\mu\nu}^a W_a^{\mu\nu}$ of the EWK Lagrangian in equation 1.21. Implementing the values of the field strength tensor $W_{\mu\nu}^a$ from equation 1.23, the relations of W_μ^\pm fields in equation 1.24, and the relations of neutral gauge fields in equation 1.27, the triple and quartic self interaction terms become,

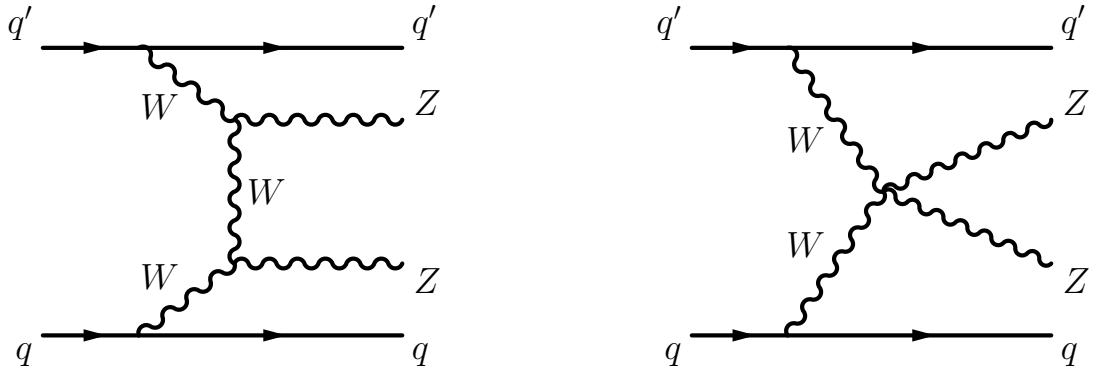
$$\mathcal{L}_3 = ie_{V=\gamma,Z}[W_{\mu\nu}^+ W^{-\mu} V^\nu - W_{\mu\nu}^- W^{+\mu} V^\nu + W_\mu^+ W_\nu^- V^{\mu\nu}] \quad (4.1)$$

$$\begin{aligned} \mathcal{L}_4 = & e_W^2 [W_\mu^- W^{+\mu} W_\nu^- W^{+\nu} - W_\mu^- W^{-\mu} W_\nu^+ W^{+\nu}] \\ & + e_{V=\gamma,Z}^2 [W_\mu^- W^{+\mu} V_\nu V^\nu - W_\mu^- V^\mu W_\nu^+ Z^\nu] \\ & + e_\gamma e_Z [2W_\mu^- W^{+\mu} Z_\nu A^\nu - W_\mu^- Z^\mu W_\nu^+ A^\nu - W_\mu^- A^\mu W_\nu^+ Z^\nu] \end{aligned} \quad (4.2)$$

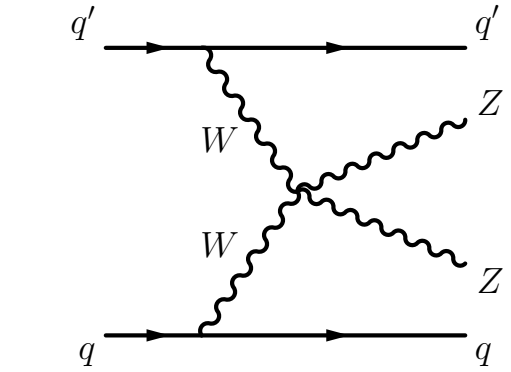
where, $e_\gamma = g \sin \theta_W$; $e_W = \frac{e_\gamma}{2\sqrt{2} \sin \theta_W}$ & $e_Z = e_\gamma \cot \theta_W$ are the precise coupling strengths for vector boson self-interaction. Both triple and quartic neutral couplings, such as ZZZ or $ZZZZ$ are absent in the SM.

Similarly, the couplings of Higgs to vector bosons are also predicted precisely by the BEH mechanism in equation 1.34 as:

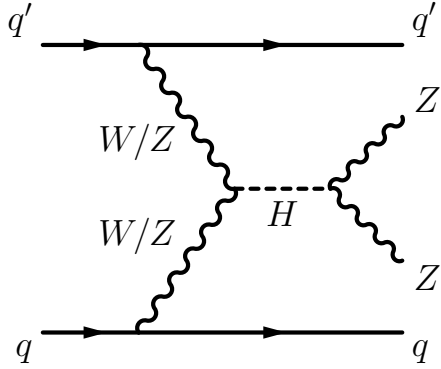
$$\mathcal{L}_{HVV} = \frac{m_W^2}{v^2} W_\mu^+ W^{-\mu} h^2 + \frac{m_Z^2}{v^2} Z_\mu Z^\mu h^2 \quad (4.3)$$



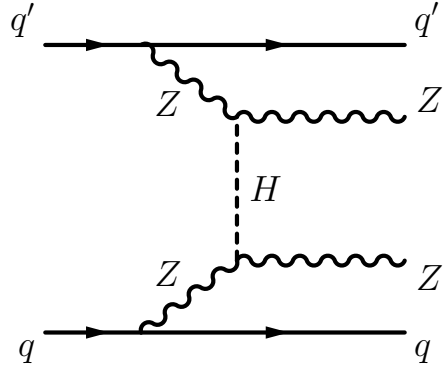
(a) ZZjj production with two triple gauge coupling (TGC) vertices.



(b) ZZjj production with a quartic gauge coupling (QGC) vertex.



(c) s-channel Higgs ZZjj Production.



(d) t-channel Higgs ZZjj Production.

Figure 6: Feynman diagrams at LO for the EWK α_{EWK}^6 production of $ZZjj$.

The EWK production of $ZZjj$ is extremely sensitive to any possible anomalous triple gauge couplings (aTGC), anomalous quartic gauge couplings (aQGC), or anomalous Higgs to vector boson coupling [26] [27] [28]. Therefore, it is imperative to probe the high energy behavior of the EWK production of $ZZjj$ to seek possible deviations from the physics processes beyond the Standard Model (BSM).

The EWK $ZZjj$ production with each Z boson decaying to a pair of same-flavor opposite-charge (SF-OC) lepton pairs is an extremely rare process. Moreover, with limited statistics in Run–2, the QCD background processes dominate the $ZZjj \rightarrow 4\ell jj$ final state [5]. Therefore,

the differential cross-sections discussed in this thesis are measured in a VBS-enhanced phase space with a high fraction of events resulting from the EWK $ZZjj$ process. The enhanced phase space relies on the characteristic feature of the EWK process with two jets (jj) in the forward-backward region originating from the scattered initial-state quarks. These jets have significant rapidity separation and no additional hadronic activity from the hard scattering between the two jets [29]. The decay of the two Z bosons into SF-OC muons or electron pairs defines the final signature of the VBS- $ZZjj$ -like event.

Chapter III: The Large Hadron Collider

5 ATLAS Detector

6 Physics Object Reconstruction

6.1 Electrons

6.2 Muons

6.3 Jets

7 Future Upgrades

Chapter IV: Analysis Overview

8 Goals

The primary goal of the analysis is to measure the differential cross-sections of the kinematic observables sensitive to the EWK $ZZjj \rightarrow 4\ell jj$ production mode. The differential cross-sections measured in VBS-enhanced phase space are used in the precision study of the SM $4\ell jj$ production and constrain the effects of BSM physics. For simpler re-interpretation in the future without ATLAS detector simulations, the differential cross-sections are measured at a particle level using an unfolding technique, which corrects the detector effects. The details of the unfolding to extrapolate the particle-level yield from detector-level yield will be discussed in Section 14. The unfolded cross-sections shown in Section 16 are then used to constrain the effect of BSM in a model-independent framework using the Effective Field Theory (EFT) approach, which will be discussed in Section 17.

9 Phase Space Definition

The unfolded differential cross-sections are measured in a phase space within the acceptance of the detector. This section summarizes the selections defining the fiducial phase space of the analysis.

9.1 Fiducial Volume

The fiducial phase space consists of events with $pp \rightarrow ZZjj \rightarrow 4\ell jj$ ($\ell = e, \mu$) with four centrally produced prompt-leptons and two jets with large rapidity gap as motivated by section 4. The fiducial phase space does not contain any leptons from the decays of unstable taus. Both particle-level electrons and muons are required to be at a dressed level. Dressed leptons in MC generators are constructed by adding the four-momenta of nearby photons emitted by the lepton within a cone size of $\Delta R < 0.1$.

To ensure the selected events fall within detector acceptance, several kinematic cuts summarized in Table 4 are applied individually to the muons, electrons, and jets before defining the event quadruplet and dijet. Each electrons are required to have $p_T > 7$ GeV and $|\eta| < 2.47$, whereas the muons satisfy $p_T > 5$ GeV and $|\eta| < 2.7$. Lepton quadruplets are formed by requiring two same-flavor, SF-OC lepton pairs, with leading and sub-leading lepton $p_T > 20$ GeV and angular separation between any two leptons to satisfy $\Delta R > 0.05$. Additionally, the invariant mass of any SF-OC lepton pair is required to satisfy $m_{\ell\ell} > 5$ GeV to suppress the contamination from lower resonance backgrounds. Based on these requirements, the quadruplets can be of the following three types:

- $4e$: events with two e^+e^- pairs.
- 4μ : events with two $\mu^+\mu^-$ pairs.
- $2e2\mu$ or $2\mu2e$: events where one of the pair is e^+e^- and other is $\mu^+\mu^-$

In any event with more than two SF-OC lepton pairs, the quadruplet is formed by choosing the two pairs that minimize the distance to the Z resonance pole. Once the quadruplet is formed, the leading-lepton pair is defined as the one with a higher absolute rapidity value, i.e., $|y_{ij}|$. Finally, an additional criterion of $m_{4\ell} > 130$ GeV is imposed on the invariant mass of the quadruplet.

Similarly, the di-jet in the fiducial phase space are also constructed from the leading-dressed jets with opposite sign of pseudo-rapidity (η) to imitate the detector-level VBS di-jet production where jets are reconstructed on the opposite side of the detector. The jets are required to satisfy $|n| < 4.5$, $p_{T, \text{leading jet}} > 40$ GeV, and $p_{T, \text{sub-leading jet}} > 30$ GeV. The di-jet is required to have a large rapidity separation of $|\Delta y_{jj}| > 2$ and $m_{jj} > 300$ GeV to resemble dijet produced in electroweak $ZZjj$ production. Table 5 summarizes the requirements to select quadruplet and the di-jet in an event.

Table 4: Details of the kinematic pre-selection applied to the dressed baseline electrons, muons, and jets.

Selections	Electrons	Muons	Jets
p_T	> 7 GeV	> 5 GeV	> 30 GeV
$ \eta $	< 2.47	< 2.7	< 4.5

Table 5: Details of the selections applied to form a quadruplet and a dijet selection in the fiducial volume.

Selections	Cut
Lepton Kinematics	$P_{T, \text{leading lepton}} > 20$ GeV $P_{T, \text{sub-leading lepton}} > 20$ GeV
Pair Requirement	$\Delta R_{\ell_i, \ell_j} > 0.05$ SF-OC with $m_{\ell\ell} > 5$ GeV
Quadruplet Requirement	2 pair candidates with smallest $ m_{12} - m_Z + m_{34} - m_Z $ Leading pair: pair with highest $ y_{ij} $ Sub-leading pair: pair with lowest $ y_{ij} $ $m_{4\ell} > 130$ GeV
Di-jet Requirement	$p_{T, \text{leading jet}} > 40$ GeV $ \Delta y_{jj} > 2$ $m_{jj} > 300$ GeV

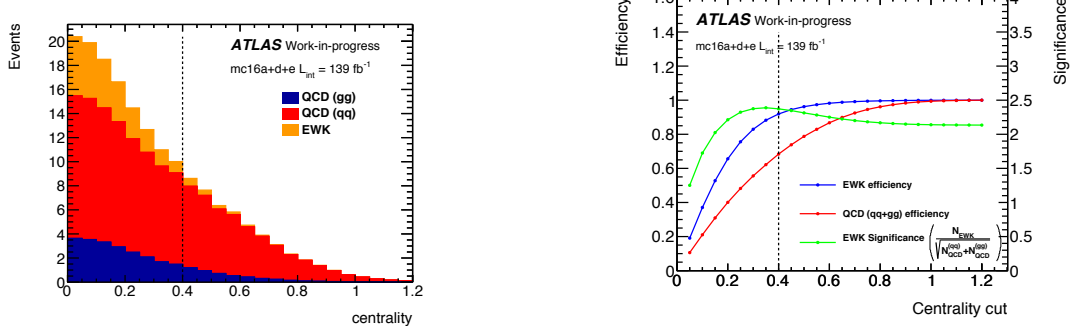
9.2 Signal Region

The signal region of the analysis is defined based on the centrality (ζ) of the di-Zboson production in an event. Centrality depends on the rapidity of the quadruplet and the rapidity of the dijet as:

$$\zeta = \frac{|y_{\text{quadruplet}} - 0.5 * (y_{\text{leading jet}} + y_{\text{sub-leading jet}})|}{|y_{\text{leading jet}} - y_{\text{sub-leading jet}}|} \quad (9.1)$$

Figure 7a shows the distribution of centrality in MC for the three main production modes of $ZZjj$. The chosen cut value on the $ZZjj$ centrality maximizes the significance of the EWK component over the inclusive qq and gg -initiated QCD production (defined as $s = \frac{N_{\text{EWK}}}{\sqrt{N_{\text{QCD}}^{(qq)} + N_{\text{QCD}}^{(gg)}}}$) while maintaining a good selection efficiency of EWK events. The second distribution in 7b shows the efficiency and significance for various cut values.

A VBS-enhanced signal region is defined based on events with a quadruplet, a dijet, and $\zeta < 0.4$. The low value of the centrality and the requirements for a signal dijet ensures that the events in this signal region originate in a more significant fraction from the electroweak production of $ZZjj$. A VBS Suppressed control region is also defined based on events with a quadruplet, a dijet, and $\zeta > 0.4$. These events mainly originate from the QCD production of $ZZjj$ and are used to optimize the analysis strategies.



(a) Yields of EWK(red) and QCD (parton initiated in blue, gg-loop initiated in green) $ZZjj$ production as a function of centrality. (b) Selection efficiency (EWK in blue, QCD in red) and EWK significance (green) for different centrality cut values. The dashed line highlights the selected cut values of 0.4.

10 Reconstruction Selection

This section summarizes the detector-level phase space selections applied to three physics objects, electrons, muons, and jets used in the measurement. Each physics object of the analysis has two categories: *baseline* and *signal* objects. Physics objects satisfying a set of kinematic selections or looser identification criteria are categorized as *baseline* whereas, the baseline leptons that pass either stricter kinematic selections or additional isolation and track-to-vertex association (TTVA) requirements are *signal*.

10.1 Electrons

As discussed in Section 6.1, electrons are reconstructed by matching the inner detector track (ID) to an energy cluster in the electromagnetic calorimeter. Baseline electron objects are required to satisfy the kinematic selections of $p_T > 7 \text{ GeV}$ & $|\eta| < 2.47$ and a loose likelihood identification of working point *LHVeryLoose*. To avoid the electrons from pileup, a loose vertex association requirement of $|z_0 \sin\theta| < 0.5 \text{ mm}$ and an overlap removal discussed in section 10.4 is applied to the baseline electron candidates.

Signal electrons are required to pass a more stringent loose likelihood identification, *LHLooseBL*, which requires at least one hit in the innermost layer of the pixel detector. The signal electrons are distinguished by requiring the baseline electrons to have impact parameter requirements of $d0/\sigma_{d0} < 5$ and an isolation working point identification of *LooseVarRad*. Table 6 summarizes the several selections imposed to define the baseline and signal electrons.

10.2 Muons

As discussed in section 6.2, muons are reconstructed in multiple ways based on information from the inner detector (ID), the muon spectrometer (MS), and the calorimeters. All baseline muons are required to satisfy $|\eta| < 2.7$, $p_T > 5 \text{ GeV}$, a loose impact parameter requirements of $|z_0 \sin\theta| < 0.5 \text{ mm}$, lepton-favoring overlap removal and *Loose* identification working

Table 6: Definition of the baseline and signal electrons.

Selection Category	Baseline	Signal
Kinematic cuts	$p_T > 7 \text{ GeV}$ $ \eta < 2.47$	$p_T > 7 \text{ GeV}$ $ \eta < 2.47$
Identification	LHVeryLoose	LHLooseBL
Vertex Association	$ z_0 \sin\theta < 0.5 \text{ mm}$	$ z_0 \sin\theta < 0.5 \text{ mm}$
Overlap removal	Lepton-favored	Lepton-favored
Isolation Working Point	—	LooseVarRad
Impact Parameters	—	$d_0/\sigma_{d_0} < 5$

point. The signal muons are identified by requiring additional isolation identification of $PflowLooseVarRad$ and TTVA requirements of $d_0/\sigma_{d_0} < 3$. Table 7 summarizes baseline and signal muons selection requirements.

Table 7: Definition of the baseline and signal muons.

Selection Category	Baseline	Signal
Kinematic cuts	$p_T > 5 \text{ GeV}$ Calo-tagged $p_T > 15 \text{ GeV}$ $ \eta < 2.7$	$p_T > 5 \text{ GeV}$ Calo-tagged $p_T > 15 \text{ GeV}$ $ \eta < 2.7$
Identification	Loose	Loose
Vertex Association	$ z_0 \sin\theta < 0.5 \text{ mm}$	$ z_0 \sin\theta < 0.5 \text{ mm}$
Overlap removal	Lepton-favored	Lepton-favored
Isolation Working Point	—	PflowLooseVarRad
Impact Parameters	—	$d_0/\sigma_{d_0} < 3$

10.3 Jets

Jets are reconstructed with the particle flow anti- K_T clustering algorithm using a radius parameter of $R = 0.4$ as discussed in section 6.3. The jets reconstructed using the particle flow algorithm are required to satisfy $p_T > 15 \text{ GeV}$, $|\eta| < 4.5$ kinematic cuts, and the lepton-favored overlap removal to be classified as baseline jets. Baseline jets satisfying the *Tight* working point of the jet to the vertex tagger tool are classified as signal jets. *Jet-vertex-tagger* (*JVT*) is applied to the baseline jets with $|\eta| < 2.4$ whereas the *forward-jet-vertex-tagger* (*fJVT*) tool is applied to the baseline jets with $|\eta| > 2.5$. Table 8 summarizes the details of

baseline and signal jets selection.

Table 8: Definition of the baseline and signal jets.

Selection Category	Baseline	Signal
Kinematic cuts	$p_T > 30 \text{ GeV}$ $ \eta < 4.5$	$p_T > 30 \text{ GeV}$ $ \eta < 4.5$
Identification	AntiKt4EMPFlow	AntiKt4EMPFlow
Overlap removal	Lepton-favored	Lepton-favored
Jet-Vertex-Tagger	– –	$ \eta < 2.4$ JVT ("Tight") $ \eta > 2.5$ fJVT ("Tight")

10.4 Overlap Removal

An *overlap removal* procedure is applied to remove the physics objects reconstructed from the same detector signal. The measurement uses a lepton-favored overlap removal which selects leptons over jets. Overlap removal is an iterative process in which only objects surviving all previous steps are used in the subsequent steps. Table 9 summarizes the overlap removal steps, where the ΔR is the angular separation between objects calculated using rapidity.

Table 9: Overlap removal used in the analysis. An object removed in one step does not enter into the subsequent step.

Remove Object	Accept Object	Overlap Criteria
Electron	Electron	Share a track or have overlapping calorimeter cluster. Keep electron with higher p_T
Muon	Electron	Share ID track, and the muon is calo-tagged
Electron	Muon	Share ID track
Jet	Electron	$\Delta R_{e-jet} < 0.2$
Jet	Muon	$\Delta R_{\mu-jet} < 0.2$ /ghost-associated and $N_{jet \text{ tracks}} < 3$

11 Event Selection

A $ZZjj$ event at the detector level consists of a lepton quadruplet formed from SF-OC baseline-lepton pairs and a dijet, passing similar selections as the fiducial level defined in section 9. The leading and sub-leading leptons are required to satisfy $p_T > 20$ GeV to ensure a high trigger efficiency. From the leptons passing these requirements, at least two SF-OC lepton pairs with $\Delta R > 0.05$ and $m_{\ell\ell} > 5$ GeV are formed. A quadruplet is formed from the two SF-OC lepton pairs whose invariant masses are closest and next closest to the mass of the Z-boson (m_Z). Similar to the fiducial level selection, the lepton pair with the highest value of absolute rapidity is identified as the leading pair. The quadruplets with all four leptons passing the signal lepton criteria of the TTVA and isolation are the *signal quadruplet* defining the signal region. While on the contrary, the quadruplets where one lepton fails either isolation or TTVA requirement used in the fake background estimation are the *not-signal quadruplets*.

A dijet in an event is selected by requiring two signal jets defined in section 10.3 from the opposite side of the detector i.e., $\eta_{lead\ jet} \times \eta_{sub-leading\ jet} < 0$). To maximize the probability of selecting an event from EWK $ZZjj$ production, a requirement of significant rapidity difference between the jets of $\Delta Y_{jj} > 2$ and a large invariant mass of $m_{jj} > 300$ GeV are imposed on the dijet selection. Table 10 summarizes all selections applied to select $ZZjj$ detector-level events.

Figure 8 illustrates a signature of two Z -bosons production in an association of two jets. The event display corresponds to an event recorded during Run Number 340368 of the 2017 data-taking period. The two light-yellow cones on two opposite sides of the detector with a large rapidity gap represent the reconstructed dijet of the event with $m_{jj} = 2228$ GeV. In this event, one of the SF-OC lepton pairs decays to e^+e^- ($Z \rightarrow e^+e^-$), and the other decays into $\mu^+\mu^-$ ($Z \rightarrow \mu^+\mu^-$).

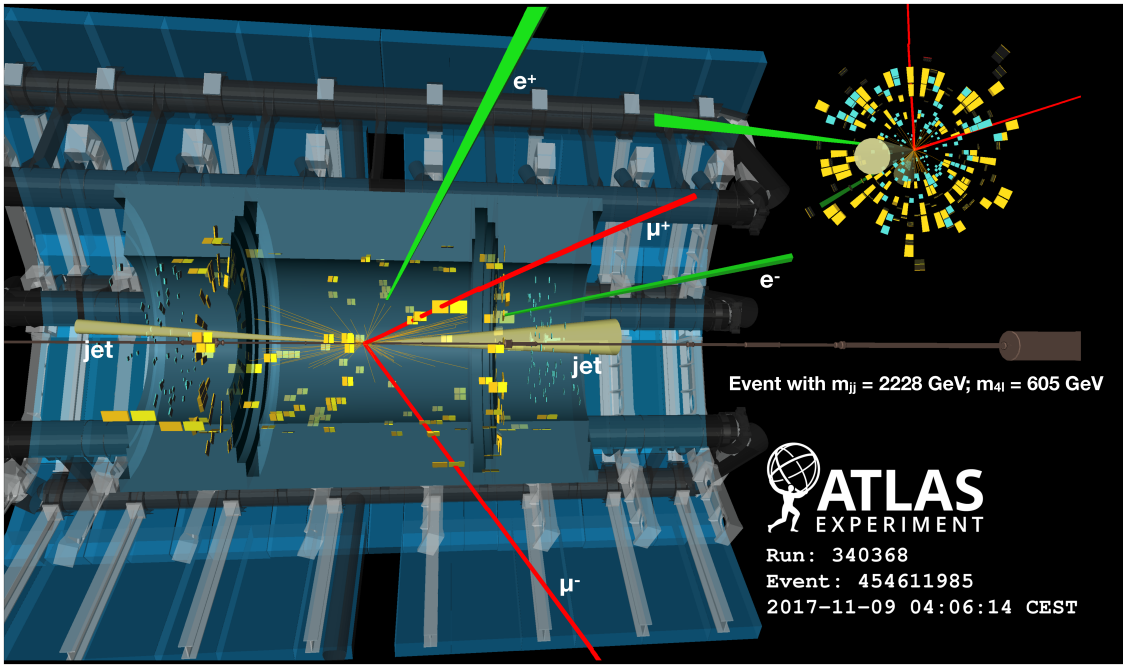


Figure 8: Event display of a candidate $pp \rightarrow ZZjj \rightarrow e^+e^-\mu^+\mu^-jj$ recorded by the ATLAS experiment in Run-2 2017 data-taking period. The invariant mass of the reconstructed four leptons is $m_{4\ell} = 605$ GeV, and that of the reconstructed di-jet is $m_{jj} = 2228$ GeV. The large rapidity separation between the two jet cones (light yellow) on the opposite sides of the ATLAS detector and centrally produced two Z bosons defines the characteristic feature of the EWK production of $ZZjj$ [5].

Table 10: Details of event selection.

Event Selection	Cut	Requirement
Event Preselection	Trigger Vertex	Fire at least one lepton trigger At least one vertex with 2 or more tracks
Quadruplet Selection	Lepton Kinematics Lepton Separation Pair Requirement Minimal Δm_Z ZZ Mass	$p_T > 20$ GeV for two leading leptons $\Delta R_{ij} > 0.05$ between leptons in quadruplet Two SF-OC lepton pairs $m_{\ell\ell} > 5$ GeV quadruplet with smallest $ m_{12} - m_Z + m_{34} - m_Z $ Leading Pair: pair with highest $ y_{ij} $ $m_{4\ell} > 130$ GeV
Quadruplet Categorisation	Signal Quadruplet Not-Signal Quadruplet	Quadruplet with all signal leptons Quadruplet with ≥ 1 baseline-not-signal lepton
Dijet Selection	Different Detector Sides Rapidity Separation Leading Jet p_T Dijet Mass Dijet	$\eta_{lead\ jet} \times \eta_{sub-leading\ jet} < 0$ $\Delta Y_{jj} > 2$ $p_{T,\ leading\ jet} > 40$ GeV $m_{jj} > 300$ GeV Both jets required to pass either JVT or FJVT
Event Categorisation	VBS-Enhanced Region VBS-Suppressed Region	signal quadruplet & dijet and centrality (ζ) < 0.4 signal quadruplet & dijet and centrality (ζ) > 0.4

The main results of the thesis are differential cross-section measurements at the particle level. The inclusive detector level cross-section for a given physics process $p_1 p_2 \rightarrow X$ is,

$$\sigma_{p_1 p_2 \rightarrow X}^{\text{detector level}} = A \times \epsilon \times \sigma_{p_1 p_2 \rightarrow X}^{\text{particle-level}} \quad (11.1)$$

where $\sigma_{p_1 p_2 \rightarrow X}^{\text{particle-level}}$ is the *true* cross-section of the physics process predicted by the theory.

The physical layout of the ATLAS detector does not cover all areas of the phase space. A accounts for the limited acceptance of the ATLAS detector. Several parts of the detector have several reconstruction efficiencies, which are accounted for by the factor ϵ . The detector level cross-section is measured experimentally in terms of the number of particles in a given final state (N) and integrated Luminosity L as $\sigma_{p_1 p_2 \rightarrow X}^{\text{detector level}} = \frac{N}{L}$. The *true* particle level inclusive cross-section can be estimated by correcting for detector acceptance and detector efficiency for the measured cross-section $\sigma_{p_1 p_2 \rightarrow X}^{\text{detector level}}$.

For differential cross-sections where the cross-section is measured in different bins of the kinematic observables, additional correction is needed to correct the resolution-induced migration between nearby bins.

This Chapter discusses the unfolding technique in detail. Section 14.1 gives an Overview of the unfolding algorithm, whereas Section 14.3 validates the unfolding method. Section 14.4 discusses the bias from unfolding and the attempts to optimize the bias.

11.1 Method Overview

The analysis uses an *iterative Bayesian unfolding* algorithm based on Baye's theorem [30]. Bayes' theorem formulates a mathematical relation to obtain a probability of an effect E caused by several independent causes C_i , given the initial probability of the causes $P(C_i)$ and the conditional probability of the $i - th$ cause to produce the effect $P(E|C_i)$ as,

$$P(C_i|E) = \frac{P(E|C_i).P(C_i)}{\sum_j P(E|C_j).P(C_j)} \quad (11.2)$$

The obtained probability depends on the prior probability of the cause and the conditional probability of cause and effect. The prior dependency is reduced by using an iterative technique, where the outcome of the previous iteration is used as a prior for the subsequent iteration.

For a single iteration, the algorithm can be summarized as,

$$U_i = \frac{1}{\epsilon_i} \times \sum_j^{reco\ bins} (R_j - F_j) \cdot f_i \cdot \frac{M_{ji} T_i}{\sum_k^{truth\ bins} M_{jk} T_k} \quad (11.3)$$

where U_i is the unfolded yield in the target bin i , T_i is the predicted truth level yield in particle bin i , R_j is the observed detector level yield in reco bin j and F_j is the subtracted detector level reducible background yield. M_{ij} is the migration matrix element from particle level bin j to detector level bin i .

Based on the discussion, conceptually, three corrections from the SM MC prediction need to be applied to estimate the unfolded yield. The three unfolding inputs are

- ***Reconstruction efficiency (ϵ)***: The reconstruction efficiency accounts for the limited acceptance and efficiency of the detector. Technically, it is defined as a fraction of events that pass both detector and fiducial level selection to the events passing only the fiducial level selection.
- ***Fiducial fraction (f)***: The fiducial fraction accounts for events that are outside the fiducial region at the particle level, which due to limited detector resolution entered in the measured distribution. An example of such an event would be a signal $4\ell + jj$ event where one of the jets originates from pile-up instead of hard-scatter. Technically, it is defined as a fraction of events that pass both detector and fiducial level selection to the events passing only the detector level selection.
- ***Migration matrix (M_{ij})***: The migration matrix is a two-dimensional matrix that accounts for events migrated from particle level bin j to detector level bin i . The migration matrix corrects the probability of bin migration. It is measured in MC by

comparing particle and detector levels distributions for events that pass both fiducial and detector-level selections. Bin migrations result from resolution effects and smearing of the reconstructed distributions. The diagonal component of the migration matrix is related to the *fiducial purity*, which corresponds to the fraction of detector-level events that originate from the same bin at the particle level.

Figure 37 show all three unfolding inputs along with the purity as a function of m_{jj} . The reconstruction efficiency is less than 50% caused by the poor jet reconstruction efficiency. The fiducial fraction and purity are smaller in lower bins of m_{jj} , which mainly corresponds to the contribution from pile-up jets faking the event selection. The normalized migration matrix shown in the second plot with the particle level prediction in *y-axis* and the detector level prediction in *x-axis* is diagonal.

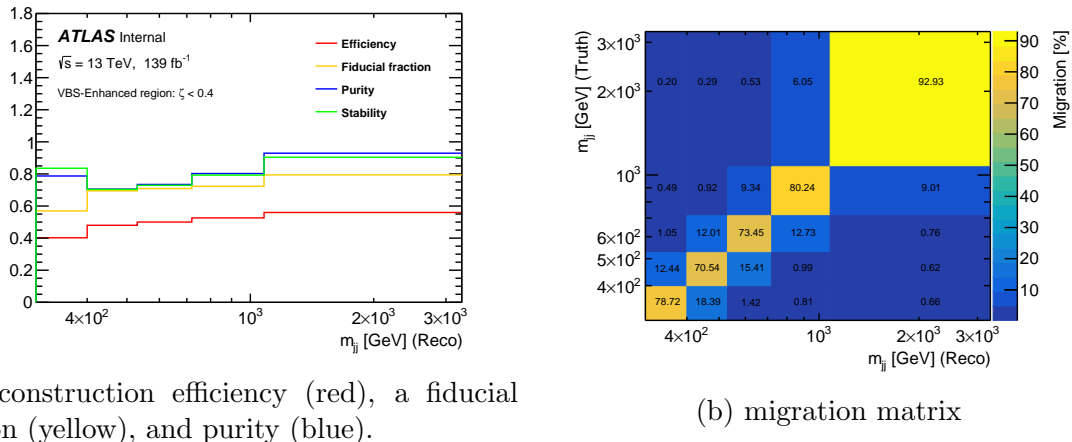


Figure 9: Unfolding inputs from SM MC as a function of m_{jj} . remake first plot with ATLAS Label and stability

11.2 Binning for Unfolding

Choosing optimal binning to perform the unfolding procedure for all kinematic observables effectively is imperative. Two factors drive the choice of binning; first, the necessity to have large enough bin statistics to maintain the Gaussian approximation while preserving the shape of the differential distributions, and second, the necessity to minimize large bin

migrations and statistical uncertainties from unfolding. Therefore, each bin must have at least 15 events in the VBS-Suppressed region and at least 20 events in the VBS-Enhanced signal region.

To maintain a good performance of the unfolding, each bin for the kinematic observable has at least 70% purity except for $p_{T,4\ell jj}$ where at least 50% purity is required. Moreover, for each observable, every bin width must be equal to or greater than the resolution of the same bin. The resolution in each particle-level bin is evaluated from MC by comparing the difference of particle and detector level yield for events that pass both fiducial- and detector-level event selection. The difference is fitted using Gaussian approximation, and twice the resulting standard deviation is taken as the resolution. Table 12 shows the final bin choices for all the kinematic observables used in differential cross-section measurement. .

11.3 Method Validation

The unfolding method is validated using three different tests.

11.3.1 MC Closure Test

The first validation of the unfolding technique is with the SM MC. An SM-predicted detector level distribution for a kinematic observable is unfolded using the unfolding inputs from the same MC. Figure 38 shows an example of the MC-based closure test for m_{jj} in the VBS-Enhanced region. The blue detector-level MC prediction is unfolded using the inputs from the same MC, and the resulting black unfolded distribution is compared with the red particle-level prediction. Since both detector-level prediction and unfolding inputs are from the same MC, a perfect closure between the unfolded and particle-level distribution is observed.

11.3.2 Injection Test

The analysis uses a model-independent EFT approach discussed in Section 17 to constrain the effect of BSM physics. Therefore, it is essential to test the ability of the unfolding

Table 11: Binning for all unfolded observables in VBS-Enhanced and suppressed regions.

Observable	Region	Binning
m_{jj} [GeV]	VBS-Enhanced VBS-Suppressed	[300, 400, 530, 720, 1080, 3280] [300, 410, 600, 178]
$m_{4\ell}$ [GeV]	VBS-Enhanced VBS-Suppressed	[130, 210, 250, 304, 400, 1130] [130, 226, 304, 752]
$p_{T,4\ell}$ [GeV]	VBS-Enhanced VBS-Suppressed	[0, 50, 80, 116, 174, 512] [0, 76, 140, 424]
$p_{T,jj}$ [GeV]	VBS-Enhanced VBS-Suppressed	[0, 52, 82, 116, 172, 524] [0, 80, 146, 448]
$p_{T,4\ell jj}$ [GeV]	VBS-Enhanced VBS-Suppressed	[0, 20, 42, 64, 298] [0, 36, 70, 254]
$s_{T,4\ell jj}$ [GeV]	VBS-Enhanced VBS-Suppressed	[70, 240, 320, 420, 580, 1410] [70, 330, 500, 1210]
$ \Delta y_{jj} $	VBS-Enhanced VBS-Suppressed	[2, 3.08, 3.74, 4.32, 5.06, 7.4] [2, 2.94, 3.78, 5.4]
$\Delta\phi_{jj}^{signed}$	VBS-Enhanced VBS-Suppressed	$[-\pi, -2.1, 0, 2.1, \pi]$ $[-\pi, 0, \pi]$
$\cos\theta_{\ell i \ell j}^*$	VBS-Enhanced VBS-Suppressed	[-1, -0.5, 0, 0.5, 1] [-1, 0, 1]
ζ	VBS-Enhanced VBS-Suppressed	[0, 0.06, 0.12, 0.18, 0.26, 0.4] [0.4, 0.5, 0.64, 1.02]

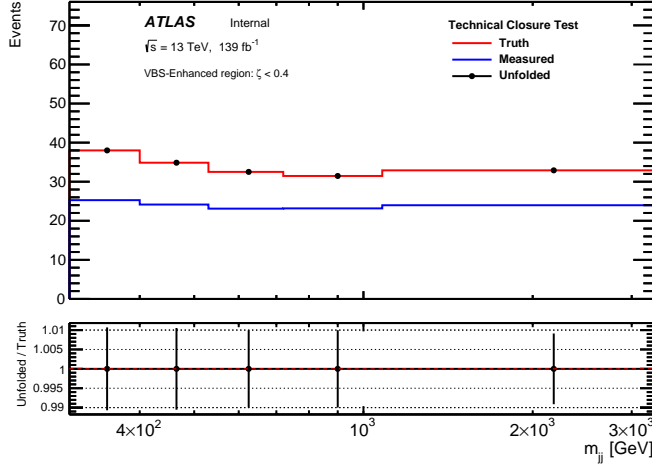
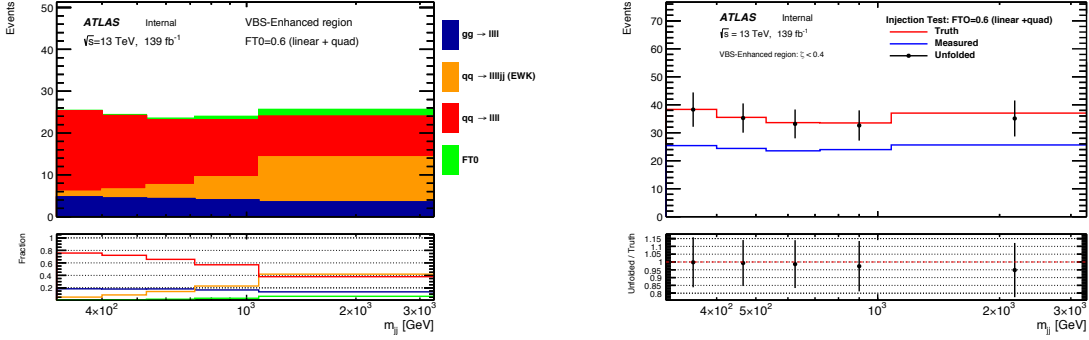


Figure 10: MC technical closure test of the unfolding procedure for m_{jj} . The detector-level MC distribution (in blue) is unfolded with the nominal SM unfolding inputs and compared to the particle-level distribution (in red) from the same MC. A perfect closure between unfolded and particle level distribution is observed

algorithm to uncover the accurate particle-level prediction from data containing BSM physics via injection test. In an injection test, a BSM physics contribution is added to the SM detector-level prediction, unfolded with the nominal SM unfolding inputs, and compared with the BSM-added particle-level distribution. Figure 39a shows an injection test for m_{jj} in the VBS-Enhanced region where a BSM contribution (green distribution) is added to the SM MC. The BSM contribution is from linear and quadratic contributions of an *FT0* EFT operator. Figure 39b shows the result of the injection test. The BSM-added detector-level MC prediction (blue) is unfolded (black) using nominal SM MC unfolding inputs and compared against the BSM-added particle-level distribution (red). A small non-closure of about 5% in the last bin of m_{jj} is observed, which is well within the uncertainties of the unfolded distribution.

Note to self: perhaps it makes sense to discuss EFT theory motivation in the theory section?



(a) Detector level MC prediction with contributions from dimension-8 $FT0$ EFT operator. (b) Unfolded SM+EFT MC detector-level distribution from dimension-8 $FT0$ EFT operator.

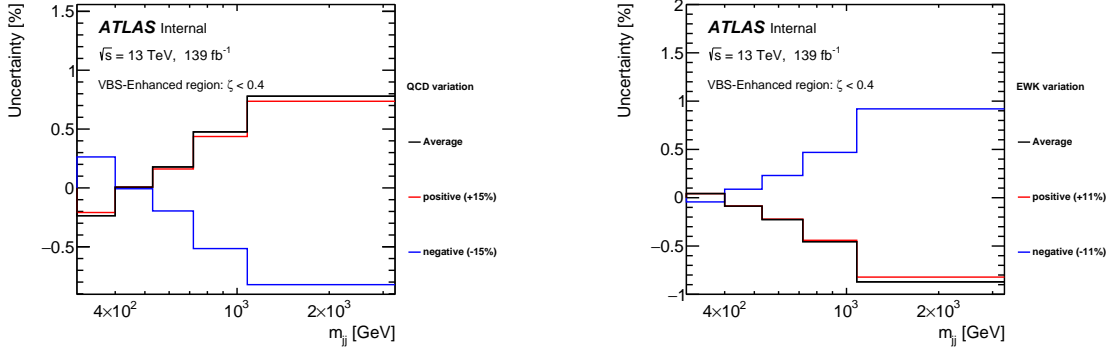
Figure 11: Injection test with dimension-8 $FT0$ EFT operator. [remake plots with ATLAS Label](#)

11.3.3 Physics Variation

From the previous ATLAS electroweak $ZZjj$ analysis, a slight enhancement on the central value of the EWk $ZZjj$ cross-section was measured [5]. The final unfolding validation tested the ability of the algorithm to recover the actual shape of particle-level distribution if a physics process cross-section was different from the SM prediction. First, as shown by figure 40a, the cross-section for parton-initiated QCD $qqZZjj$ is varied by a factor equal to the total statistical uncertainty on data in the VBS-Suppressed region $\pm 15\%$. The varied detector-level distribution is then unfolded using the nominal SM MC unfolding inputs and compared with the varied fiducial level prediction. Figure 40b shows the same test where the $EWKqZjj$ cross-section is varied by $\pm 11\%$ based on the enhanced cross-section observed in the previous measurement. In both cases, a non-closure of about 1% is observed, well below the uncertainties from unfolding.

11.4 Bias and Optimization

The unfolded procedure relies on a prior value depending on the SM MC, which naturally biases the unfolded cross-sections. With each iteration of unfolding, the algorithm improves



(a) QCD cross-section is varied by $\pm 15\%$ (b) EWK cross-section is varied by $\pm 11\%$

Figure 12: Unfolding validation using physics variation where parton-initiated QCD (left) or the EWK process cross-sections are varied.

the knowledge of the prior, thus, reducing the unfolding bias. However, with an increasing number of iterations, the repeated bin migrations amplify the statistical fluctuations in data, resulting in larger values of statistical uncertainties. Therefore, a finite number of iterations is chosen, and the resulting unfolding bias is taken as the systematic uncertainty for the measurement.

The unfolding bias is evaluated by the *data-driven closure test*, where a pseudo dataset is developed utilizing the ratio of observed data and SM-predicted detector-level yield. First, for each observable, the data and MC ratio are smoothed using Friedman's Super Smoother technique [], fixing the endpoints to the value of the ratio in the first and last bins. A reweighing function for each observable is developed to reweigh the SM fiducial- and detector-level yields. The reweighed detector-level signal yield is then unfolded with the nominal unfolding inputs from SM and compared with the reweighed fiducial-level yield to get the final unfolding bias. Figure 41 shows a step-by-step procedure for the data-driven closure test. As shown by the ratio panel of figure 41d, unfolding bias of order 10% is observed.

The bias observed in figure 41d is obtained using one number of iterations for unfolding. The data-driven closure test was repeated for several iterations to reduce the unfolding bias. The resulting unfolding bias and systematic uncertainties up to 4 iterations are shown in figure 42. As expected, the unfolding bias decreases, whereas the statistical uncertainty

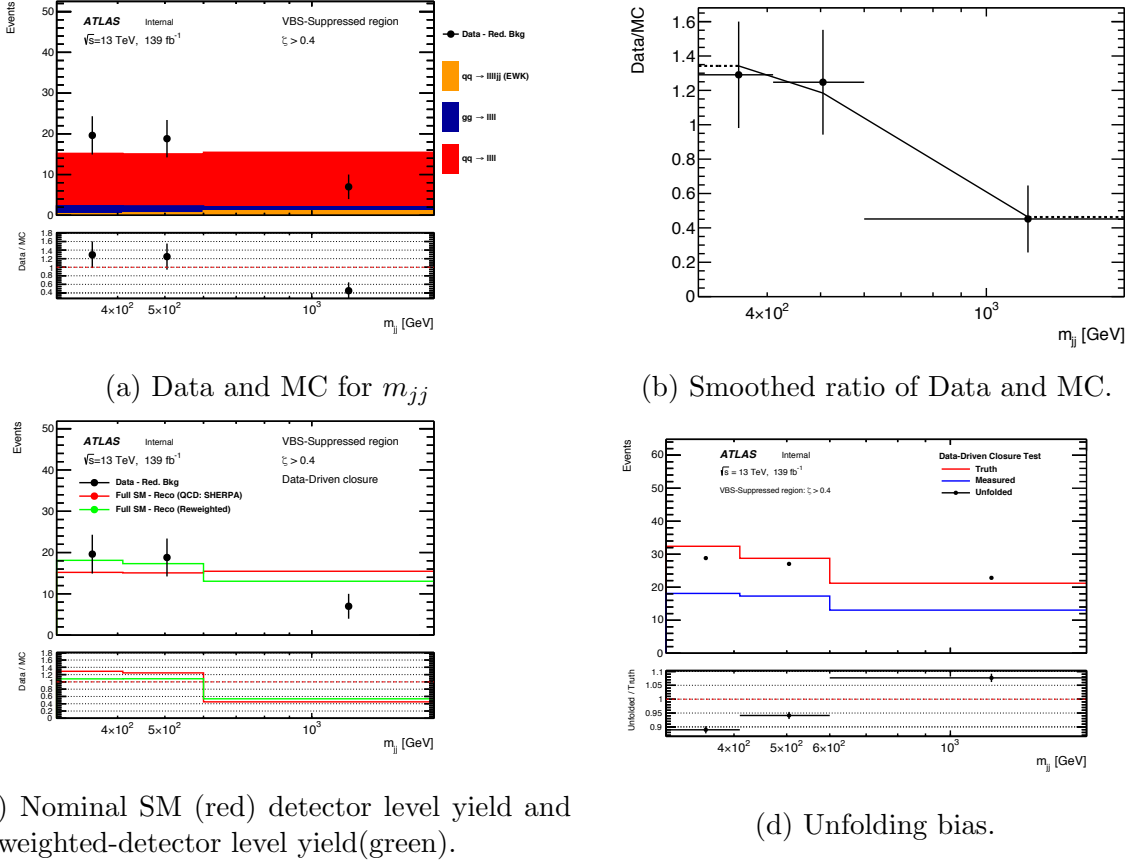


Figure 13: A step-by-step overview of the data-driven closure test to get the unfolding bias. remake plots with ATLAS Label

increases with the higher number of iterations. One number of iterations is chosen as the optimal in the measurement to balance the statistical and bias uncertainty.

Unfolding bias is the largest source of the systematic uncertainty of the analysis and is studied in detail using MC-driven toy studies to understand the source. The observed significant bias is from detector-level pile-up jets at lower p_T or higher η that are not part of the fiducial phase space. The jet-vertex-tagger and forward-jet-vertex-tagger have lower efficiency in selecting the hard scattering jets at lower p_T or higher η , thus resulting in more *fiducial-fake-event* contamination. The additional MC-based studies on the unfolding bias are summarized in Appendix B.

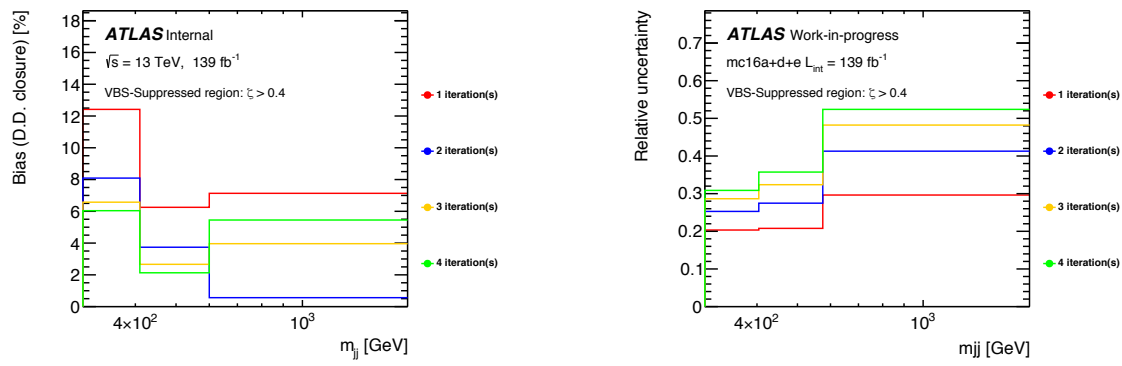


Figure 14: Unfolding bias (left) and statistical uncertainty (right) with up to 4 unfolding iterations as a function of m_{jj} in VBS-Suppressed region.

12 Definition of Measured Observables

The primary results of the thesis are differential cross-sections of the following 11 different kinematic observables:

- $m_{4\ell}$: invariant mass of the four-leptons (or 2 Z -bosons)
- m_{jj} : invariant mass of the dijet
- $p_{T,4\ell}$: transverse momentum of the four-leptons
- $p_{T,jj}$: transverse momentum of the dijet
- $p_{T,4\ell jj}$: transverse momentum of the four-leptons and the dijet
- $s_{T,4\ell jj}$: scalar transverse momentum of the four-leptons and the dijet
- $\Delta\phi_{jj}^{signed}$: difference in the azimuthal angle between the two jets in the dijet, ordered according to their rapidity,i.e.

$$\Delta\phi_{jj}^{signed} = \begin{cases} \phi(j_1) - \phi(j_2) & \text{if } y_{j_1} > y_{j_2} \\ \phi(j_2) - \phi(j_1) & \text{otherwise} \end{cases}$$

- Δy_{jj} : the absolute value of rapidity difference between the leading and the sub-leading jets in the dijet
- ζ : centrality of the system
- $\cos\theta_{\ell 1 \ell 2}^*$: cosine of the decay angle of the negative lepton of the leading pair in the pair's rest frame as shown by figure 15
- $\cos\theta_{\ell 3 \ell 4}^*$: cosine of the decay angle of the negative lepton of the sub-leading pair in the pair's rest frame as shown by figure 15

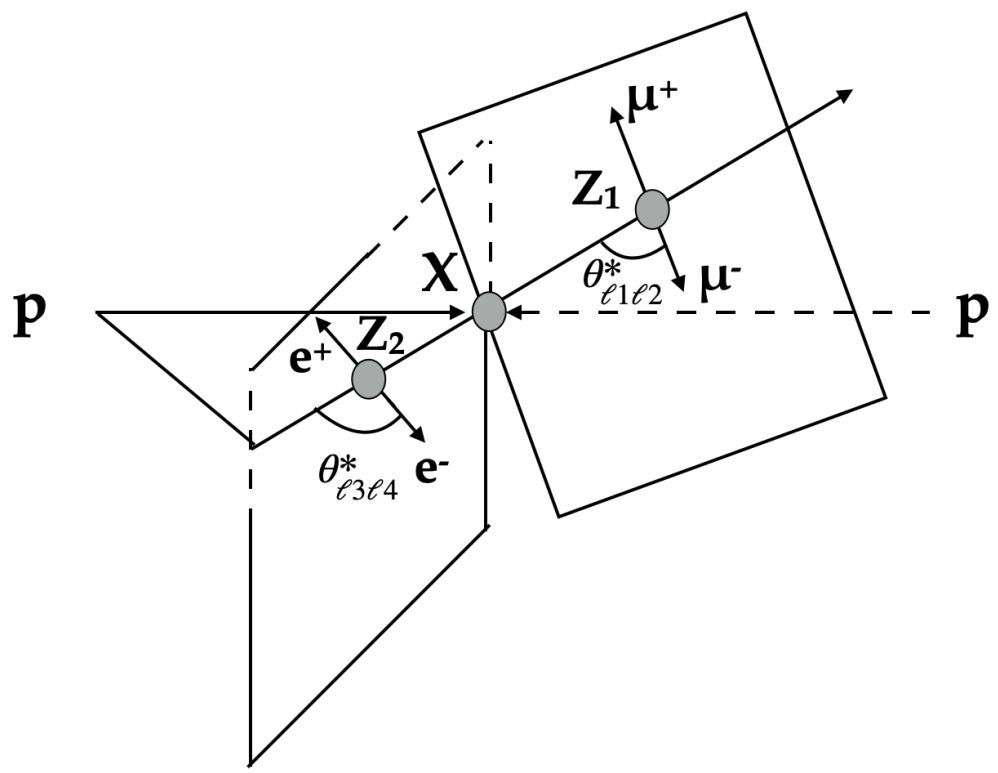


Figure 15: Figure showing the decay angle $\theta_{\ell 1 \ell 2}^*$ ($\theta_{\ell 3 \ell 4}^*$) of the negative lepton in the primary (secondary) pair's rest frame. [6].

Chapter v: Analysis Strategy

13 Background Estimation

13.1 Data Driven Estimate of Fake Background

Non-prompt leptons originate from a non-hard scatter source, either from a secondary interaction such as jet decay or from charged tracks misidentification. Figure 16 shows an example of non-prompt lepton production. The hard scatter process produces a b-jet which in secondary interaction produces a muon whose track does not point towards the interaction vertex and is surrounded by jet activities. The signal lepton criteria of isolation and TTVA discussed in Section 10 discards most of the non-prompt leptons. However, some non-prompt leptons pass the signal criteria and, in association with other prompt leptons, form a quadruplet in the signal region. Thus, giving rise to the *fake background* events for the analysis. The origins of non-prompt leptons are discussed in detail in Section 13.1.1.

The fake backgrounds could be predicted using the MC for $Z(\rightarrow \ell\ell) + jets$, $t\bar{t}$ and WZ processes where one or more non-prompt leptons in association with the prompt leptons form a signal quadruplet. However, the MC predictions of the fake background events are statistically limited. It is challenging to precisely model the non-prompt leptons originating from the reconstruction effects. Therefore, the fake backgrounds are estimated using an entirely data-driven technique discussed in this Section. Figure 17 shows the schematic of the whole background estimation process. The fake factors are evaluated from a combined control region (CR), formed by combining two independent control regions $Z + jets$ and $t\bar{t}$. Both regions are enriched in non-prompt leptons, and the combination is discussed in Section 13.1.2. Section 13.1.3 discusses the technical aspects of the fake factor method, and Section 13.1.4 discusses the fake efficiencies. The fake background is estimated by applying

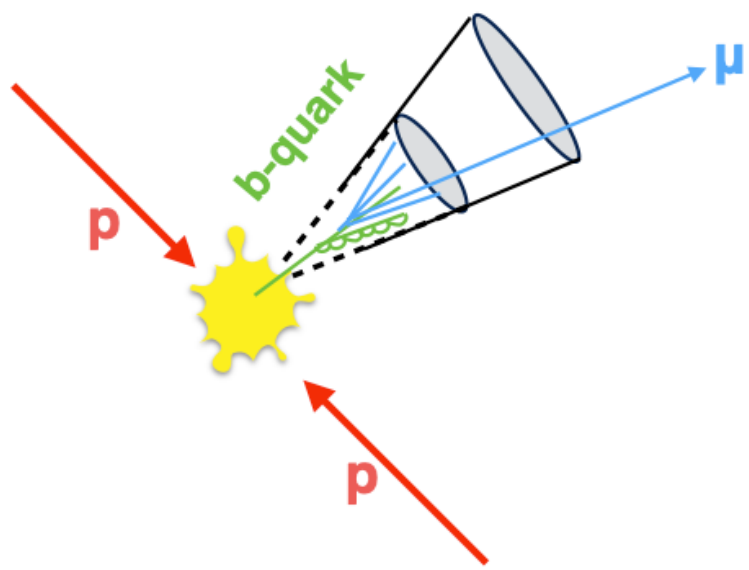


Figure 16: A schematic of the non-prompt lepton production from secondary interaction. Jet activities surround the non-prompt muon, and the muon track does not point to the hard scatter interaction point.

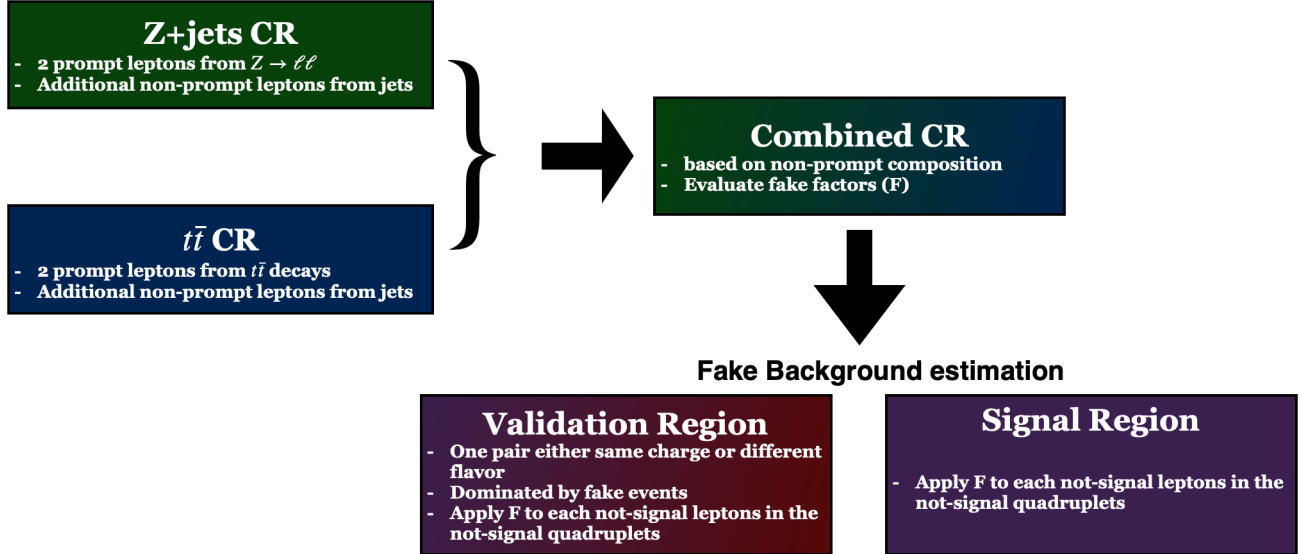


Figure 17: An overview of the fake background estimation.

the fake factors to each anti-signal lepton in not-signal quadruplets. First, the background estimation technique is validated in fake-enriched validation regions discussed in Section 13.1.5 and applied to the signal region, which is discussed in Section 13.1.6.

13.1.1 Lepton Composition

The fake background MC predictions provide essential insight into the origin of the non-prompt leptons. A classification tool developed by the Isolation and Fake Forum (IFF) identifies the true origin of the leptons, which is studied to understand the composition of non-prompt leptons in various phase-space regions of the analysis ¹. The tool has the

¹<https://gitlab.cern.ch/atlas/athena/-/tree/21.2/PhysicsAnalysis/AnalysisCommon/TruthClassification>

following classification of truth origin for a non-prompt lepton

- *Unknown or KnownUnknown*: leptons with insufficient truth-level information to be classified by the tool.
- *IsoElectron*: electrons originate either from the hard scatter or a boson decay. These electrons are treated as prompts in signal and background control regions.
- *ChargeFlipIsoElectron*: electrons whose charge is mismeasured at detector level and is classified as a non-prompt.
- *PromptMuon*: muons originate from either the hard scatter or a boson decay. These muons are treated as prompts for signal and background control regions.
- *PromptPhotonConversion*: non-prompt electrons originating from photon conversion.
- *TauDecay*: leptons originating from tau decays are treated as prompt leptons.
- *BHadronDecay*: leptons originating from hadrons containing a b-quark. These types of leptons are one of the primary sources of non-prompt leptons.
- *CHadronDecay*: leptons originating from hadrons containing a c-quark.
- *LightFlavourDecay*: leptons originating from mesons and lighter hadrons.

Figure 18 shows the origin of all leptons that are part of the quadruplet in the events with a signal quadruplet and a dijet. Most of the leptons in these regions are prompt and predominantly originate from $gg \rightarrow ZZjj$, $qq \rightarrow ZZjj$, and $EWKqq \rightarrow ZZjj$ processes. The leptons are classified *Unknown/KnownUnknown* due to insufficient truth information and mainly originate from $t\bar{t}Z(\rightarrow \ell\ell)$ and VVV processes. The event record lacks information on the intermediary bosons for these samples, thus failing to identify the lepton origin. The *Unknown/KnownUnknown* leptons are treated as prompt leptons in the signal region. This treatment relies on the fact that ΔR between the *Unknown/KnownUnknown*

classified truth leptons and reconstruction level lepton is observed to be close to 0. The *Unknown/Known* classified leptons are treated as non-prompt leptons in the background control regions.

Figure 19 shows the fraction of non-prompt electrons (left) and non-prompt muons (bottom) in the events with a signal quadruplet and a dijet. The non-prompt leptons originating from b -hadrons or c -hadrons are collectively called *heavy flavor (HF)* non-prompt leptons. All other non-prompt leptons are categorized as *light flavor (LF)* non-prompt leptons. About 50% of non-prompt electrons in the signal region originate from heavy flavor sources, whereas more than 90% of non-prompt muons originate from the heavy flavor decays.

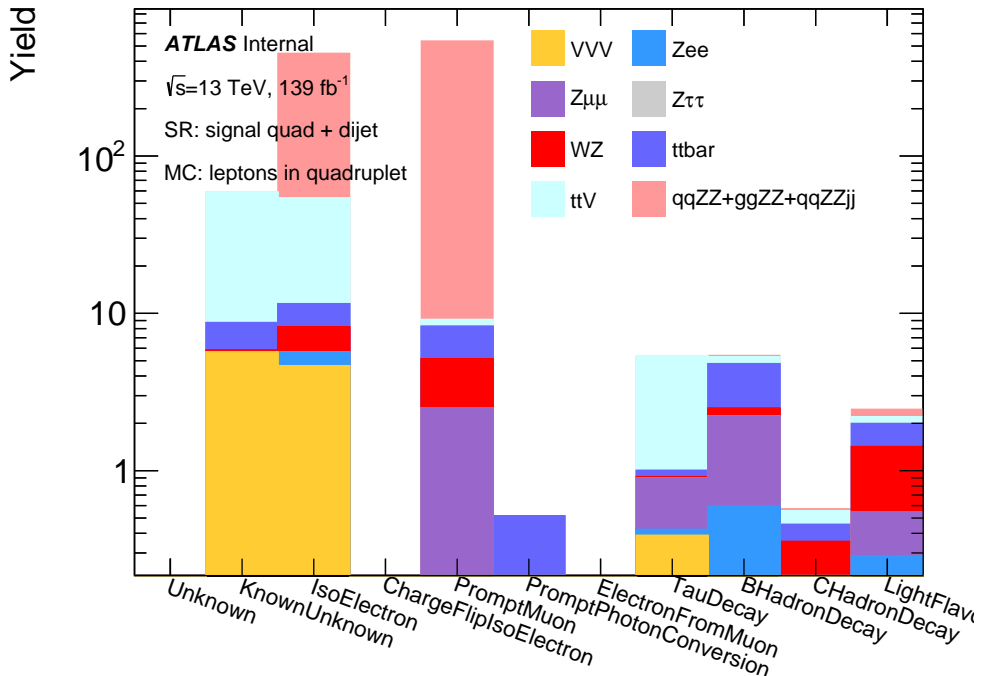


Figure 18: Origins of leptons in the signal region in events with a quadruplet and a dijet. The lepton origin is classified by the IFF classifier tool. Only leptons that are part of the signal quadruplet are shown. [remake plots with label and larger y-axis](#)

13.1.2 Control Regions

The fake factors are measured from data in a fake enriched background control region formed by combining two independent control regions, the $Z + jets$ control region and the $t\bar{t}$ control

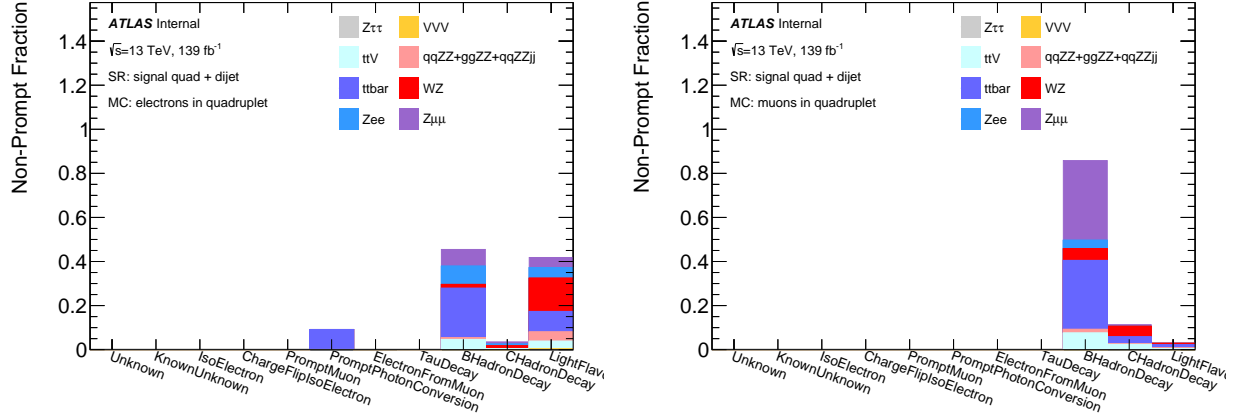


Figure 19: Origins of non-prompt leptons in the signal region in events with a signal quadruplet and a dijet. The events are normalized to the number of non-prompt electrons (left) and non-prompt muons (right). [remake plots w/wo ATLAS label](#)

region. Events in the control regions consist of a prompt lepton pair from a physics process and additional leptons from non-prompt sources. Both control regions use a single or dilepton trigger similar to the signal region and require the leading and sub-leading leptons in an event to satisfy $p_T, \text{leading lepton} > 20 \text{ GeV}$ and $p_T, \text{sub-leading lepton} > 15 \text{ GeV}$. An event in the $Z + jets$ CR consists of an SF-OC prompt-lepton pair from the Z boson decay with an invariant mass of $76 \text{ GeV} < m_{\ell\ell} < 106 \text{ GeV}$, and additional leptons. Additionally, no events can have missing transverse energy higher than 50 GeV to suppress the contamination from the WZ process.

Similarly, the $t\bar{t}$ CR consists of events with different flavor prompt-lepton pairs and additional leptons. An event in the $t\bar{t}$ CR requires at least one b-tagged jet to reduce the WZ contamination. The b-tagging in the $t\bar{t}$ CR is performed by a flavor tagging tool described in Ref [31].

Figure 20 shows the fractions of the additional baseline electrons (left) and muons (right) that originate from a non-prompt source as a function of their p_T in the $Z + jets$ CR (blue) and the $t\bar{t}$ CR (red). A high fraction ($\geq 80\%$) of baseline electrons originate from non-prompt sources in both $Z + jets$ CR and $t\bar{t}$ CR. More than 95% of the low- p_T baseline muons are from non-prompt sources in both control regions. These distributions show that

most of the additional leptons in either control region are expected to be from non-prompt sources, thus, motivating the control regions to evaluate the fake factors.

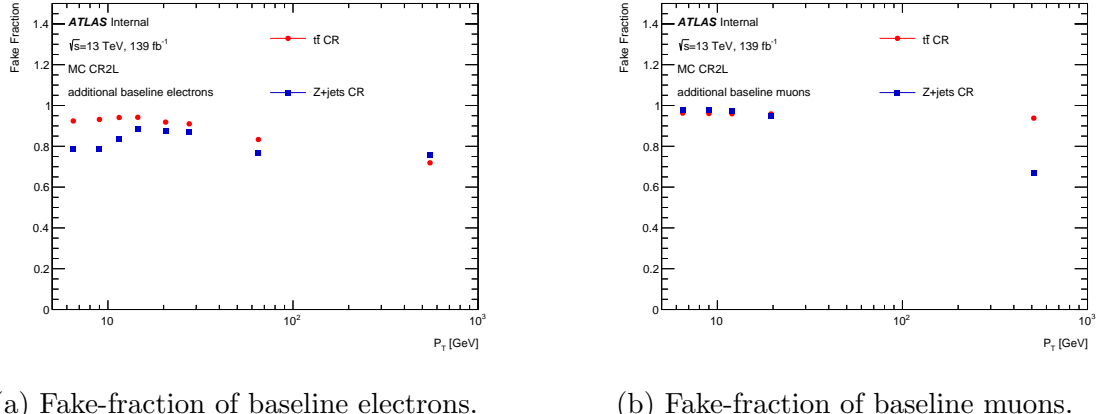
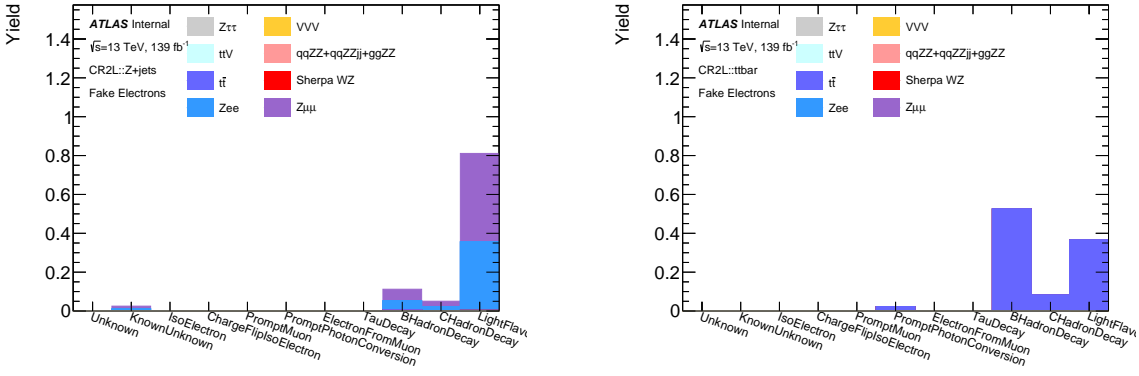


Figure 20: Fraction of non-prompt electrons and muons in the $Z + jets$ and $t\bar{t}$ control regions.
remake plots w/wo ATLAS label

The control regions have a unique non-prompt lepton composition as shown by figures 21 and 22. More than 80% of the non-prompt electrons in the $Z + jets$ CR originate from the light flavor decays, but about 60% are from the light flavor decays in the $t\bar{t}$ CR. Similarly, about 80% of the non-prompt muons in the $Z + jets$ CR originate from the heavy flavor, whereas more than 90% are from the heavy-flavor decays in the $t\bar{t}$ CR. The non-prompt compositions of the signal region shown in figure 19 are different from either control region. The two independent control regions are combined to form a single control region with a similar non-prompt lepton composition as the signal region.

The b -jet requirement applied to suppress the prompt-lepton contamination from the WZ process in $t\bar{t}$ CR ensures the presence of at least one jet in all events. Therefore, events without jets in the combined control region only contain the $Z + jets$ $n_{jet} = 0$ events. The two control regions are first weighted and combined for the events with the jets to match the heavy flavor composition of the $n_{jet} > 0$ events in the signal region. The combination weights are evaluated by solving the following equation:

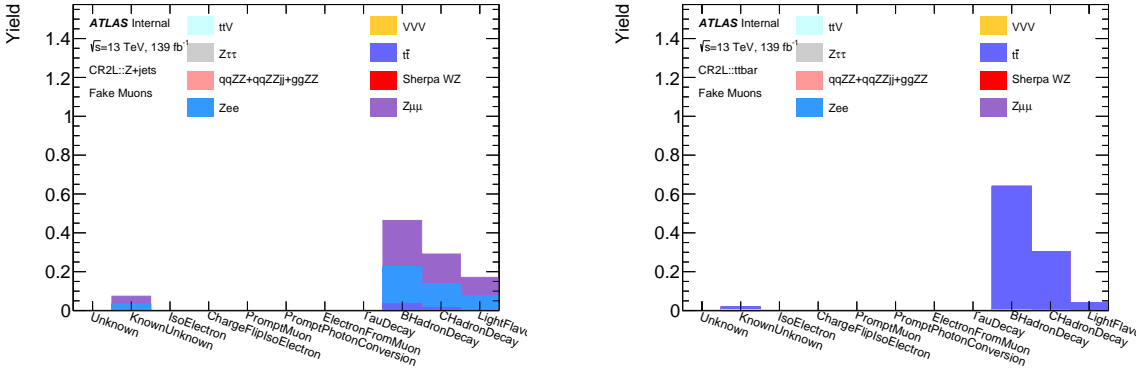
$$\frac{\{w \times N_{Z+jets} \times f_{HF,Z+jets}\} + \{(1-w) \times N_{t\bar{t}} \times f_{HF,t\bar{t}}\}}{\{w \times N_{Z+jets} + (1-w) \times N_{t\bar{t}}\}} = f_{HF,SR} \quad (13.1)$$



(a) Non-prompt electrons in $Z + jets$ CR.

(b) Non-prompt electrons in $t\bar{t}$ CR.

Figure 21: Sources of non-prompt electrons in background control regions. Fake composition is unique in these control regions. remake plots w/wo ATLAS label



(a) Non-prompt muons in $Z + jets$ CR.

(b) Non-prompt muons in $t\bar{t}$ CR.

Figure 22: Sources of non-prompt muons in $Z + jets$ (left) and $t\bar{t}$ (right) control regions. remake plots w/wo ATLAS label

where N is the total yield in the control region, f_{HF} is the ratio of the non-prompt leptons from heavy-flavor decays to total non-prompt leptons, and w is the combination weight to be determined.

As the composition of non-prompt electrons and muons are different in different regions, the weights are evaluated separately for electrons and muons and evaluated as $w_\mu = 0.26$ and $w_e = 0.06$. Figure 23 shows the composition of the non-prompt electrons and muons in the combined control region, which is formed by a weighted combination of the $Z + jets$ CR and the $t\bar{t}$ CR.

Figure 24 shows the distributions of additional baseline electrons as a function of their

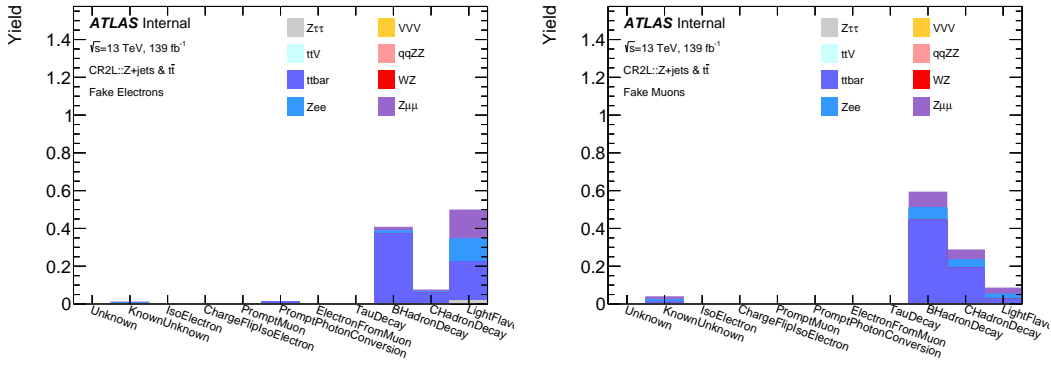


Figure 23: Origins of non-prompt electrons (left) and muons (right) in the combined control region. **remake plots w/wo ATLAS label**

p_T in the $Z + jets$ CR (left) and $t\bar{t}$ CR (right). The bottom distribution shows the same for the combined control region. For $Z + jets$ CR at low p_T region, additional baseline electrons are overestimated in MC by about 20% showing the limited precision of the MC to estimate the non-prompt leptons. Similarly, figure 25 shows the distributions of additional baseline muons as a function of their p_T in the three control regions. In $Z + jets$ CR, additional muons mainly originate from $Z \rightarrow \ell\ell$ process in low p_T region, whereas at high p_T contribution from $t\bar{t}$ and WZ is more significant.

13.1.3 Fake Factor Strategy

The centrally developed *fake factor tool* by ATLAS IFF is used to estimate the fake background [32]. The tool takes the ratio of signal to baseline leptons, i.e., *fake efficiency* (f), calculated in the combined control region as an input where,

$$f = \frac{N_{\text{non-prompt signal leptons}}}{N_{\text{non-prompt baseline leptons}}} \quad (13.2)$$

For a simple case of a signal region with one signal lepton, the observed signal lepton (N^T) and baseline-anti-signal lepton (N^L) can be estimated in terms of the number of prompt or real baseline leptons (N_R^B) and the number of non-prompt or fake baseline leptons (N_F^B) as

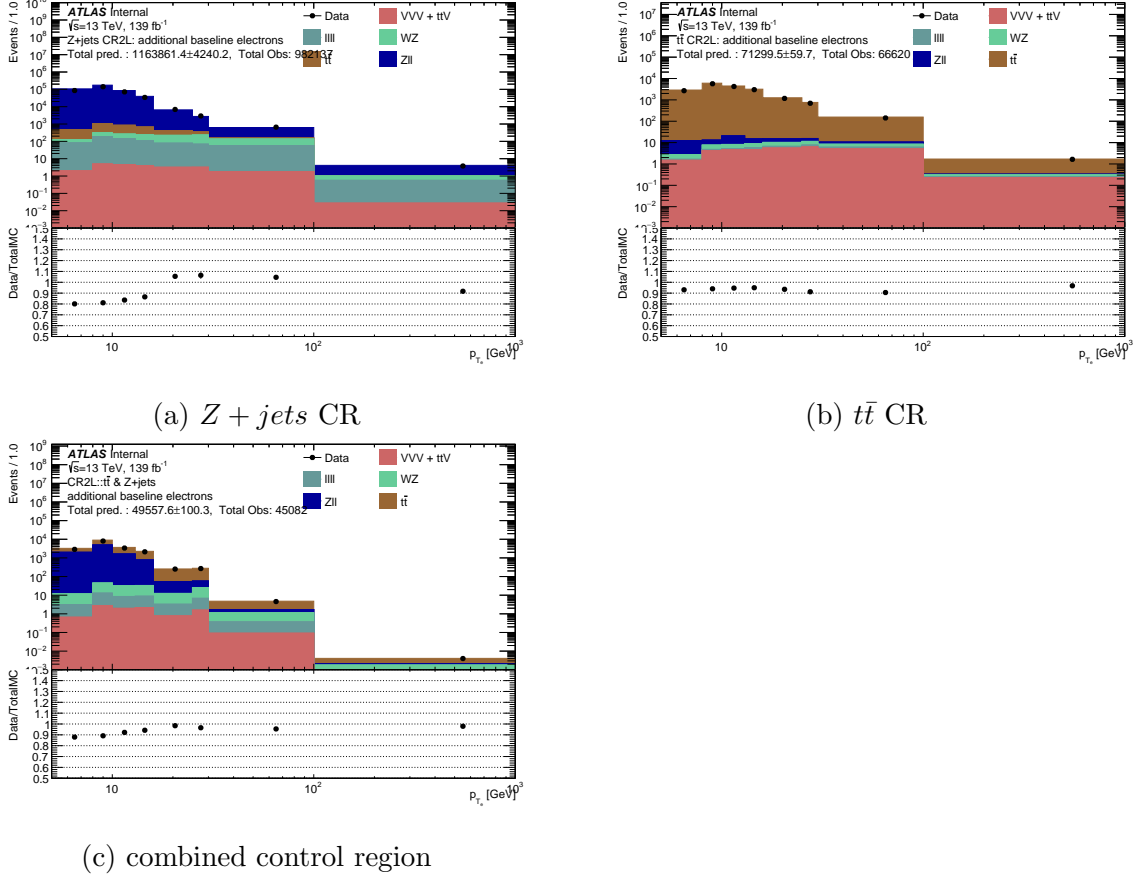


Figure 24: Additional baseline electrons as a function of p_T in control regions. **remake plots w/wo ATLAS label**

$$N^T = rN_R^B + f_F^B \quad (13.3)$$

and

$$N^L = (1 - r)N_R^B + (1 - f)N_F^B \quad (13.4)$$

where, r is the *real efficiency* such that,

$$r = \frac{N_{\text{prompt signal leptons}}}{N_{\text{prompt baseline leptons}}} \quad (13.5)$$

Equations 13.3 and 13.4 can be written as a 2×2 matrix equation as

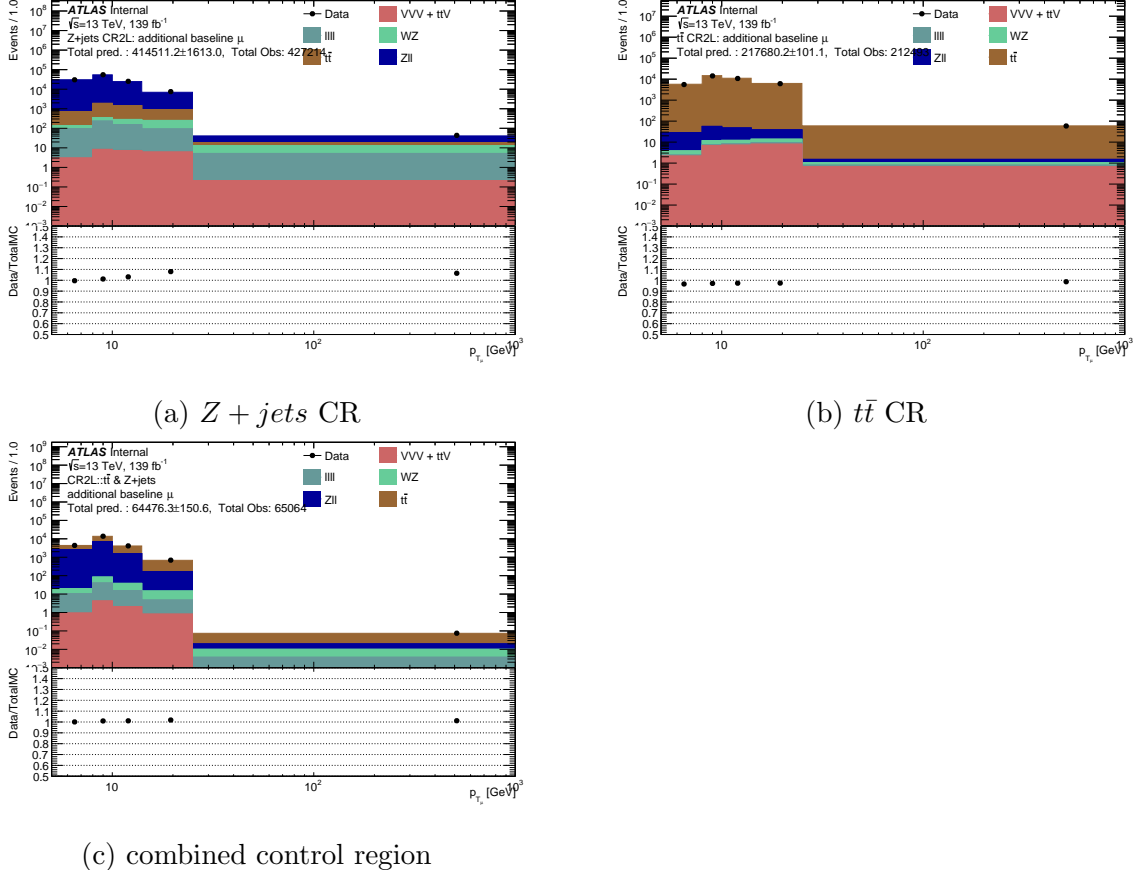


Figure 25: Additional baseline muons as a function of p_T in control regions. **remake plots w/wo ATLAS label**

$$\begin{pmatrix} N^T \\ N^L \end{pmatrix} = \begin{pmatrix} r & f \\ 1-r & 1-f \end{pmatrix} \begin{pmatrix} N_R^B \\ N_F^B \end{pmatrix} \quad (13.6)$$

The number of non-prompt baseline contributions is estimated by ignoring the higher-order term of the fake efficiency as

$$N_F^B = \frac{1}{r-f} [r(N^T + N^L) - N^T] \quad (13.7)$$

Therefore, the predicted number of non-prompt signal leptons is

$$N_F^T = \frac{f}{r-f} [r(N^T + N^L) - N^T] \quad (13.8)$$

The fake factor method assumes the $r \rightarrow 1$ limit, which simplifies equation 13.8. However, since the real efficiency of any measurement is less than one, this approximation overestimates the fake background. To account for this overestimation, the number of genuine baseline-anti-signal prompt leptons (N_R^L) are measured in MC and subtracted to get the final background yield as,

$$N_F^T = \frac{f}{1-f} [N^L - N_R^L] \quad (13.9)$$

The method makes a typically safe assumption that the real anti-signal prompt leptons are modeled precisely in MC. The coefficient F is the fake factor where,

$$F = \frac{f}{1-f} \quad (13.10)$$

As the fake efficiency f is estimated from data in the combined control region, the fake factor background estimation method does not rely on any efficiencies or yield in the tight signal region.

This method can be extended to the four-lepton signal region where there are four baseline leptons, of which one or more could be non-prompt. Corresponding to the permutation of individual leptons to be either signal or baseline-anti-signal, there are $2^4 = 16 \{N^{TTTT}, N^{TTTL}, N^{TTLL}, \dots, N^{LLLL}\}$ observations to consider. The analysis considers N^{TTTT} the signal region; therefore, the background is estimated from the quadruplets with at least one baseline-anti-signal lepton.

13.1.4 Fake Efficiency & Systematics

Fake efficiency (f), defined in previous Section 13.1.3, is evaluated from the combined control region using the total number of additional leptons from data as

$$f = \frac{N_{Data}^{Signal} - N_{MC}^{Prompt Signal}}{N_{Data}^{Baseline} - N_{MC}^{Prompt Baseline}} \quad (13.11)$$

Since some additional leptons could originate from prompt sources, such contributions are estimated from MC and subtracted as shown in equation 13.11.

Figures 20, 24, and 25 show that the fake-fraction and the total yield of the additional leptons are dependent on their transverse momentum p_T . Therefore, the fake efficiency evaluated using equation 13.11 depends on the lepton p_T . Because of the low resolution of the detector in forward regions, a higher number of non-prompt leptons are expected; thus, the fake efficiency depends on the leptons' pseudorapidity η . Additionally, since the non-prompt leptons predominantly originate from jets, the fake efficiency also depends on the number of jets n_{jets} in an event.

Figures 26 and 27 show the fake efficiencies for electrons and muons respectively as a function of p_T (top-left), η (top-right) and n_{jets} (bottom-center). Since high- p_T leptons are most likely to originate from a prompt source, fake efficiency typically decreases as a function of p_T for leptons. The dependency on η is most likely from lower detector resolution causing a higher number of misidentifications and lower efficiency for TTVA.

As discussed in Section 10.4, the lepton-favored overlap removal used in the analysis rejects jets if they overlap with leptons. Due to the $b - jet$ requirement in $t\bar{t}$ CR, the $n_{jet} = 0$ events only consist of contributions from the $Z + jets$ CR, which does not have an explicit event requirement on the number of jets. The probability of non-prompt leptons passing the isolation requirement is higher in events with no jets or surrounding hadronic activity. Therefore, as observed, a higher fake efficiency is expected in events without jets.

The fake efficiency is parametrized in three-dimensional distributions of p_T , η , and n_{jets} . Only two bins ($n_{jet} = 0$ & $n_{jet} > 0$) are used for number of jets. The distributions in figure 28 show the fake efficiency of an electron as a function of p_T & η for $n_{jet} = 0$ bin (left) and for $n_{jet} > 0$ bin (right). Similar distributions are shown in figure 29 for muons.

The fake efficiency distributions' binomial errors are propagated as the statistical uncertainties on the fake estimate. The subtracted prompt component of equation 13.11 is estimated using MC predictions. As discussed in Section 3, the prediction relies on the

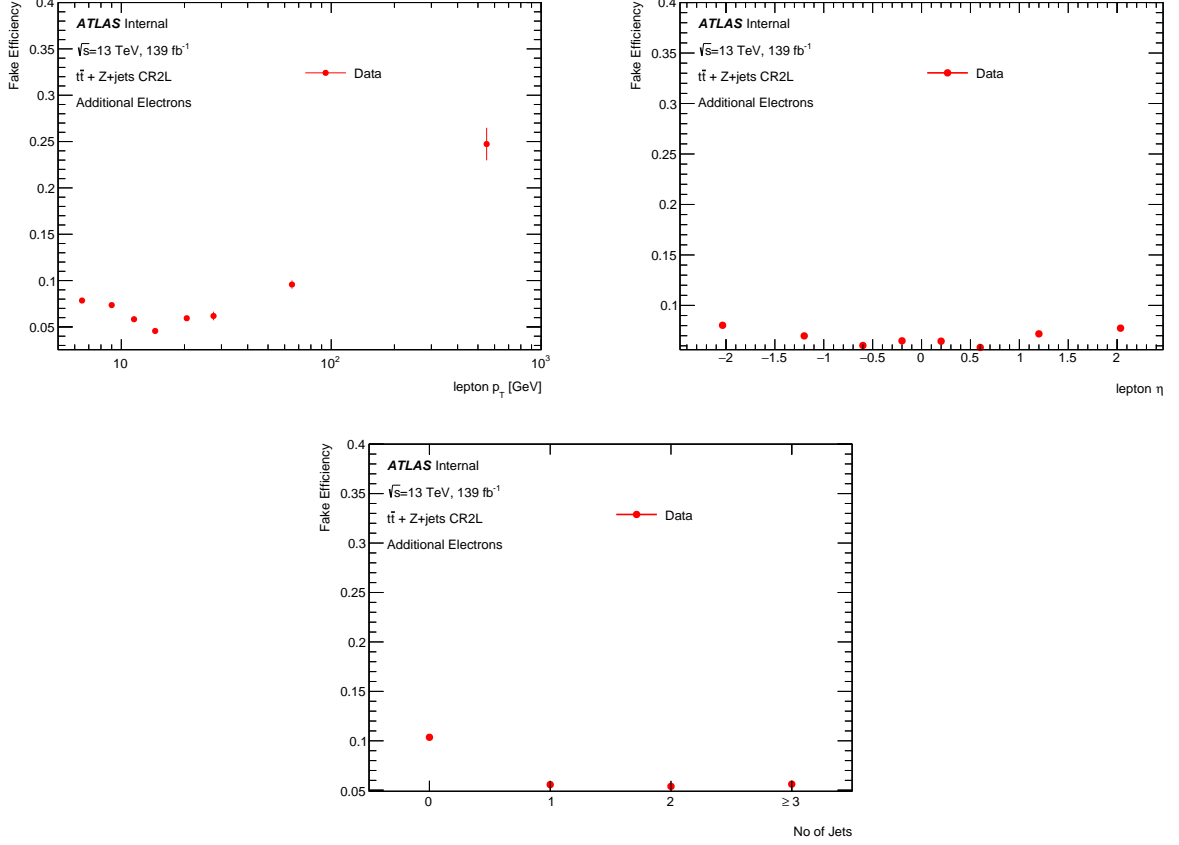


Figure 26: Fake efficiency of fake electrons measured in the combined control region from data as a function of its p_T , η , and n_{jets} . [remake plots w/wo ATLAS label and change color](#)

PDF, the energy-dependent QCD factorization and renormalization scale, and the strong coupling constant (α_S). Therefore, the theory uncertainties on these three parameters are propagated as systematic uncertainties of the fake efficiency.

For each theory uncertainty, a variation-applied fake efficiency is evaluated by separately varying the numerator and denominator of the fake efficiency equation 13.11. The difference between the variation-applied fake efficiency and the nominal fake efficiency is considered systematic uncertainty. Figures 30 and 31 show the statistical and systematic uncertainties on the fake efficiency calculated in the combined control region. For both electrons and muons, the statistical uncertainty is dominant.

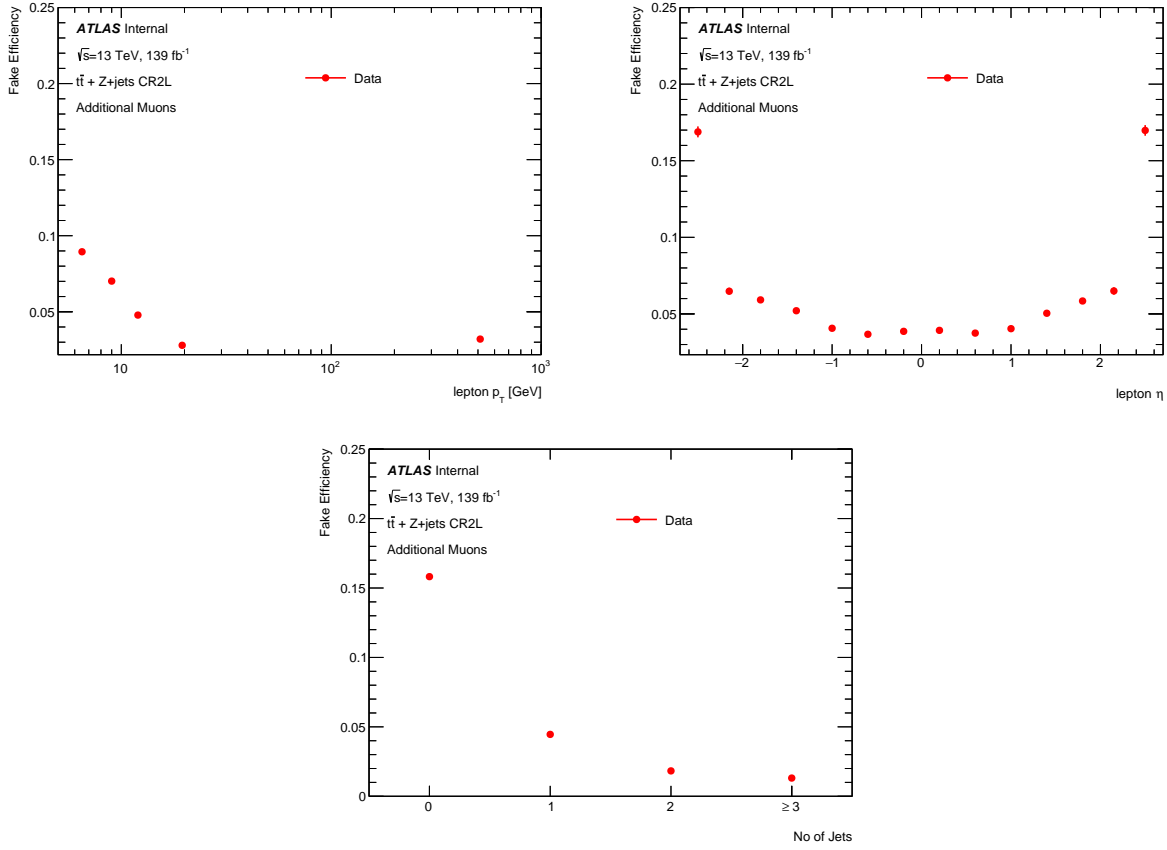


Figure 27: Fake efficiency of fake muons measured in the combined control region from data as a function of its p_T , η , and n_{jets} . **remake plots w/wo ATLAS label and change color**

13.1.5 Method Validation

Before implementing the fake-factor method to estimate the fake background in the signal region, the method is validated in two separate validation regions

1. Different-flavor validation region (VRDF): one pair in the quadruplet must have two different-flavor leptons.
2. Same-charge validation region (VRSC): one pair in the quadruplet must have two same-charge leptons.

The low statistics in both regions result from requiring one of the pairs to be either same-charge or different-flavor. Therefore, events in the validation regions only have a signal

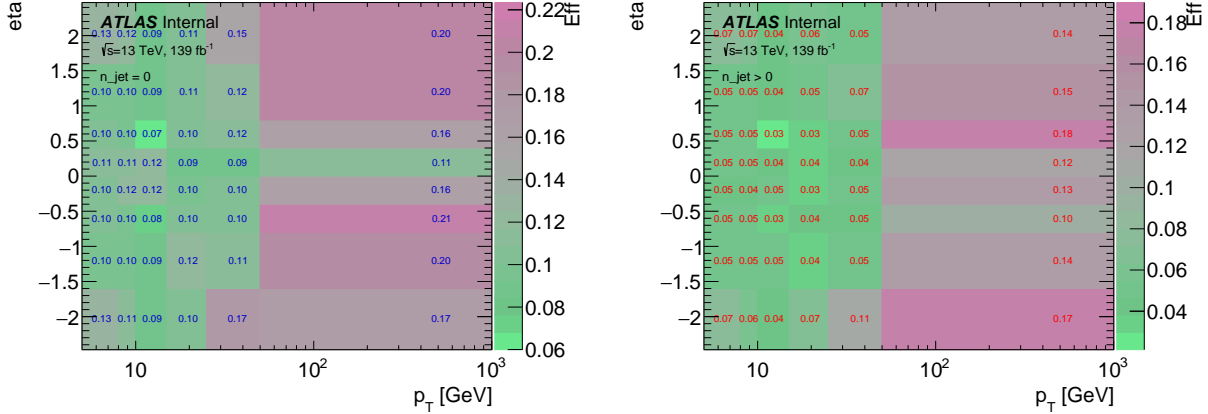


Figure 28: Fake efficiency of fake electrons measured in the combined control region from data as a function of its p_T , and η in two slices of n_{jets} ($n_{jet} = 0$ left) and ($n_{jet} > 0$ right).
remake plots w/wo ATLAS label, change the color of text for second plot and y-label

quadruplet without any dijet requirement. The validation regions’ quadruplets are formed by requiring the same kinematic criteria as that of the signal region discussed in Section 11. The trigger requirement, object selection, and overlap removal are identical to the signal region. Additionally, events in the VRDF are required not to have any b-tagged jet to reduce the contribution from $t\bar{t}Z$ processes. Reducing the $t\bar{t}Z$ component further reduces the significant modeling uncertainties related to the $t\bar{t}Z$ process.

By constructing either a same-charge or a different-flavor pair, the event yield in validation regions is dominated by events where at least one lepton in the quadruplet is a non-prompt-signal lepton known as the fake background in the signal region. The events also originate from other physics processes, such as $qqZZ$, $qqZZjj$, $ggZZ$, $t\bar{t}Z$, and VVV whose contribution is predicted by the same MC generators as that of the signal region.

Figures 32 show the non-prompt composition in the different flavor validation region (left) and same-charge validation region (right). The non-prompt compositions in the two validation regions are different from that of the signal region or the background control regions composition as shown in figures 19, 21 and 22. Therefore, to validate the fake background estimation strategy, it is imperative to observe a good correspondence between data and a combination of the MC prediction with the fake background yield in both validation regions.

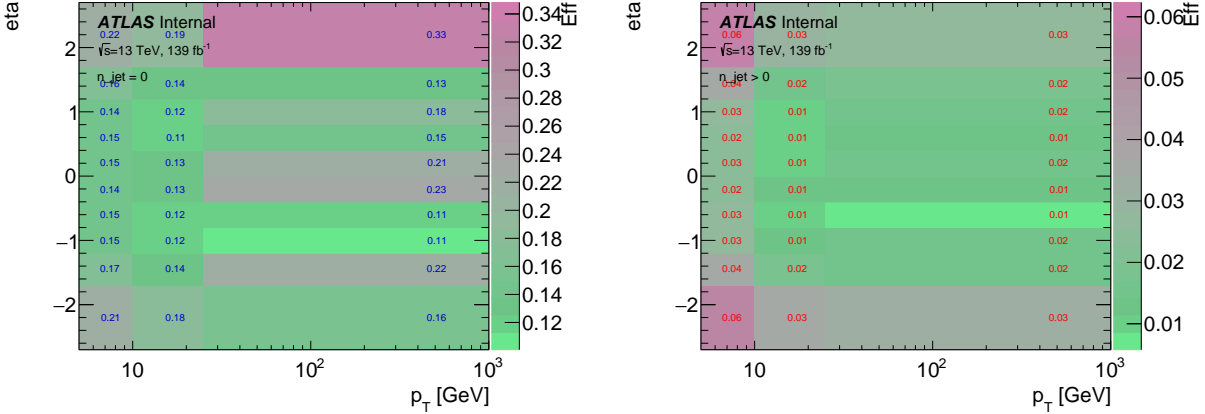


Figure 29: Fake efficiency of fake muons measured in the combined control region from data as a function of its p_T , and η in two slices of n_{jets} ($n_{jets} = 0$ left) and ($n_{jet} > 0$ right).
remake plots w/wo ATLAS label, change the color of text for second plot and y-label

The fake backgrounds for the validation regions are estimated by applying the fake factor to each baseline-anti-signal leptons in the not-signal quadruplet, as discussed in Section 13.1.3. Figure 33a shows the data and the predicted MC yield in VRDF as a function of $m_{4\ell}$ where the fake backgrounds are estimated from $Z + jets$, $t\bar{t}$, and WZ MC predictions. Figure 33b shows the same but the reducible estimated using the fake factor method. Similarly, figures 33c and 33d show the yields as a function of $m_{4\ell}$ in the same charge validation region. Both regions have similar characteristics, and the fake background dominates the event yield with some contribution from other physics processes.

The systematic gray bands in figures 33b and 33d include the systematic and statistical uncertainties from the fake factor method, as well as the uncertainties on PDF, QCD scale, and strong coupling (α_s) on the $qqZZ$, $qqZZjj$ & $ggZZ$ MC prediction. The bands also include the uncertainties in the cross-section measurements of the ttZ and VVV processes. The treatment of the systematic theoretical uncertainties is the same as that of the signal region and will be discussed in Section 15.1. Other experimental uncertainties related to the lepton reconstruction and identification, trigger, and luminosity discussed in Section 15.2 are assumed to be negligible for the validation regions. For most bins, the data and MC yield are compatible with both regions' systematic and statistical uncertainties. Moreover,

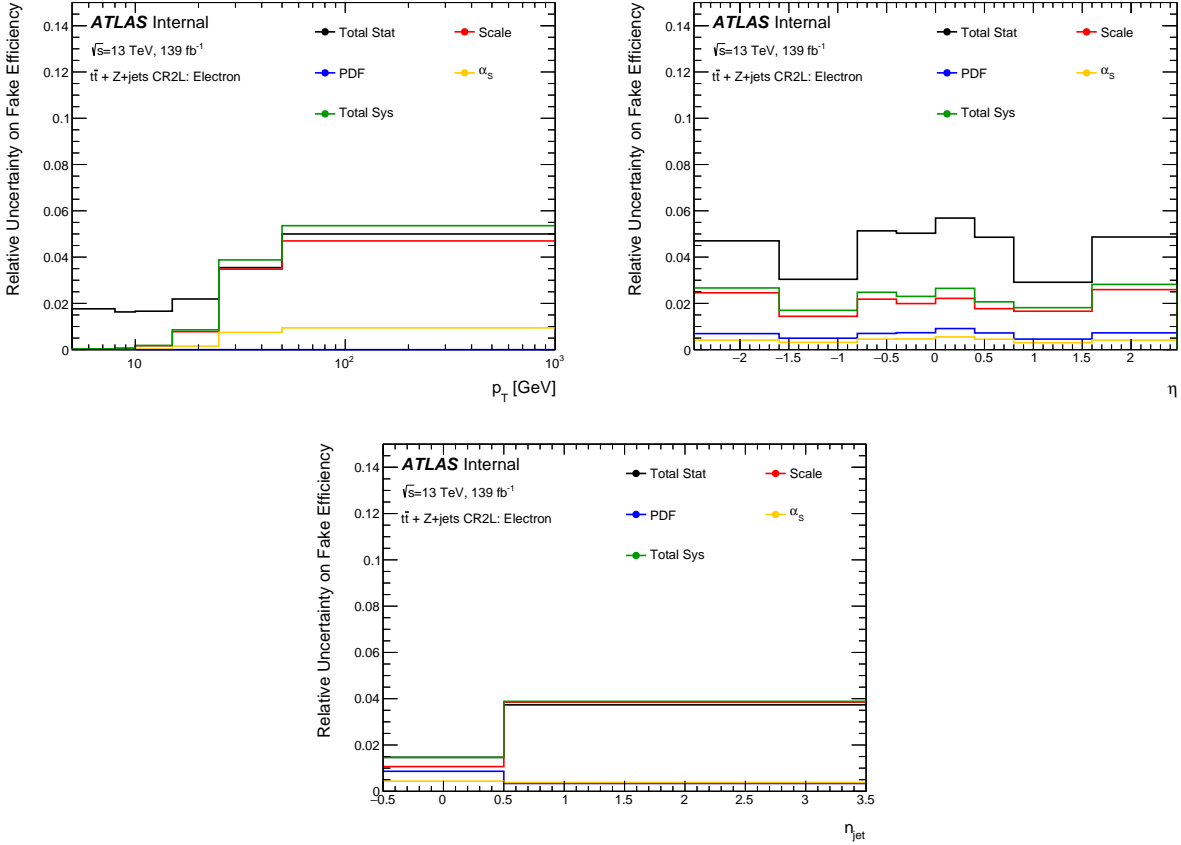


Figure 30: Uncertainties on the fake efficiency of the fake electrons measured in the combined control region from data as a function of its p_T , η , and n_{jets} . remake plots w/wo ATLAS label

the agreement between data and MC simulation is better when the reducible events are estimated using the fake factor method, thus, fully validating the method.

The data and MC yield comparisons for several kinematic observables in VRDF (left) and VRSC (right) are shown by distributions in figure 34. The data and MC prediction are compatible in most bins within the systematic uncertainties for all the observables.

13.1.6 Signal Region Estimation

Similar to the validation regions, the background in the signal region is estimated by applying the fake factor to the not-signal quadruplets, as discussed in section 13.1.3. Distributions in figure 35 compare the fake background predicted from MC and estimated from the fake-

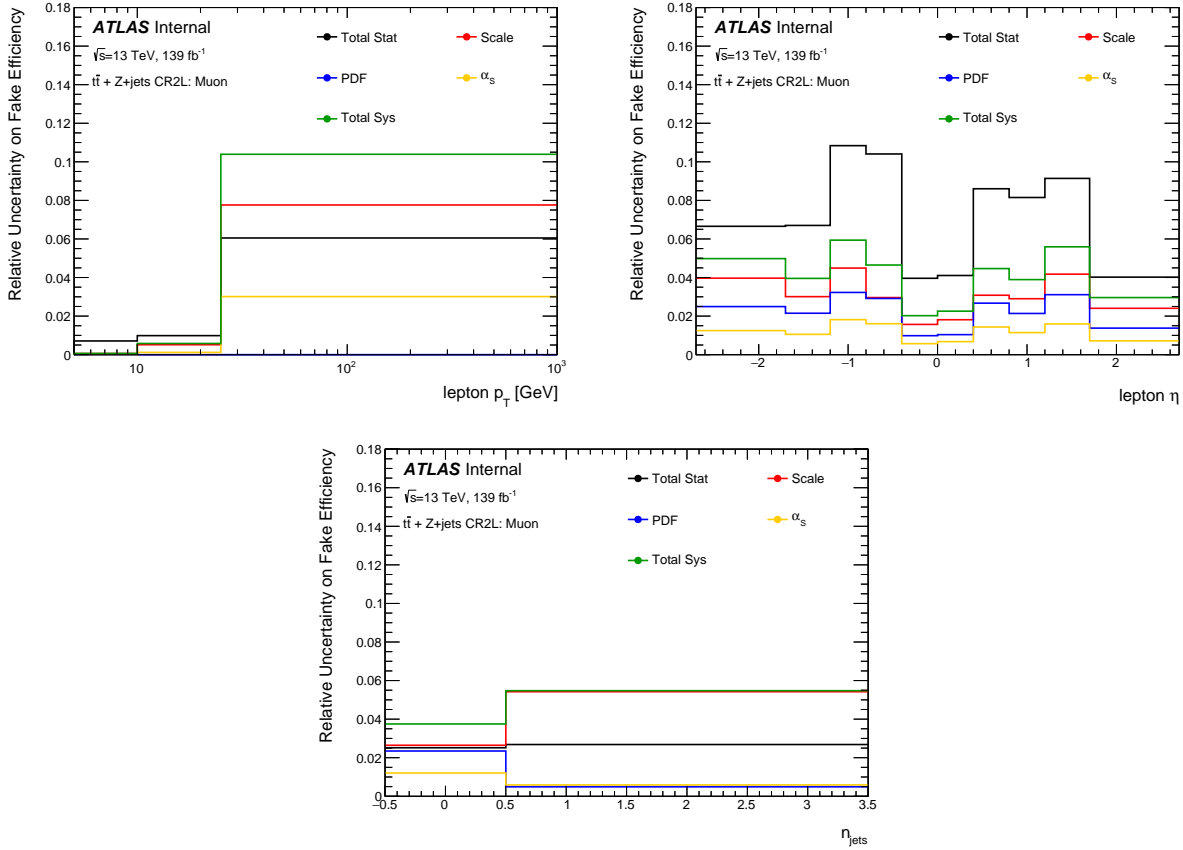


Figure 31: Uncertainties on the fake efficiency of the fake muons measured in the combined control region from data as a function of its p_T , η , and n_{jets} . **remake plots w/wo ATLAS label**

factor method in the VBS-Enhanced signal events as a function of $m_{4\ell}$ (left) and $p_{T,4\ell}$ (right).

Figure 36 shows identical distributions but also includes the total SM prediction in the same region. The lower panel of the plot shows the fake background to the predicted signal ratio, which is small. The gray bands in the plots are from systematic uncertainties of the fake factor method, whose effect is negligible on the overall yield of the signal region.

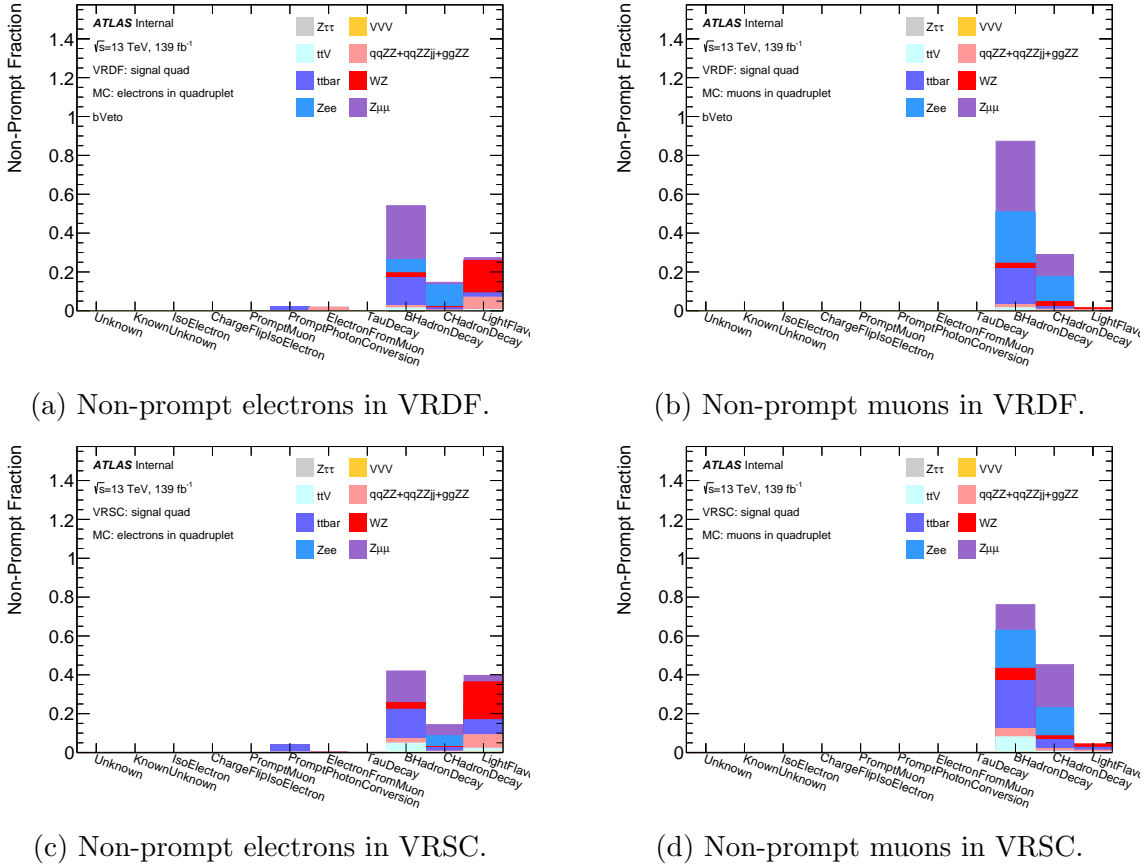
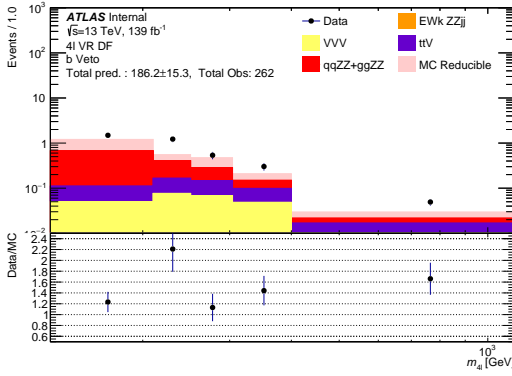
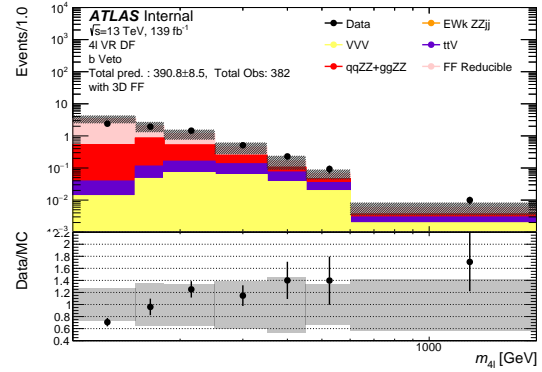


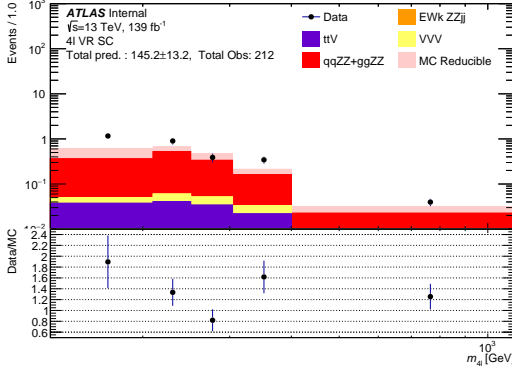
Figure 32: Sources of non-prompt electrons and muons in the different flavors and the same charge validation regions.
remake plots with ATLAS Label



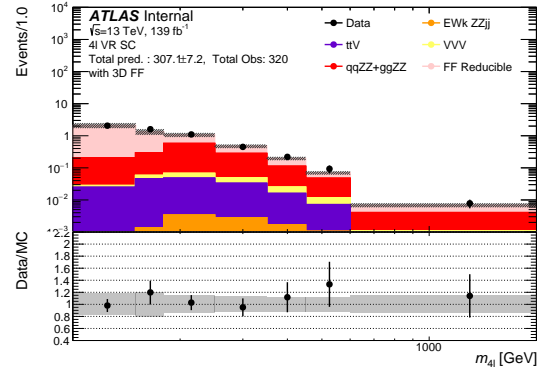
(a) VRDF: MC predicted fake background.



(b) VRDF: data-driven fake factor estimate of fake background.



(c) VRSC: MC predicted fake background.



(d) VRSC: data-driven fake factor estimate of fake background.

Figure 33: Yield as a function of $m_{4\ell}$ in the different flavor (top) and same charge (bottom) validation regions. In both regions, the MC prediction matches more closely with data when the fake background events are estimated using the data-driven fake-factor method. [remake plots with ATLAS Label and cleaning other labels](#)

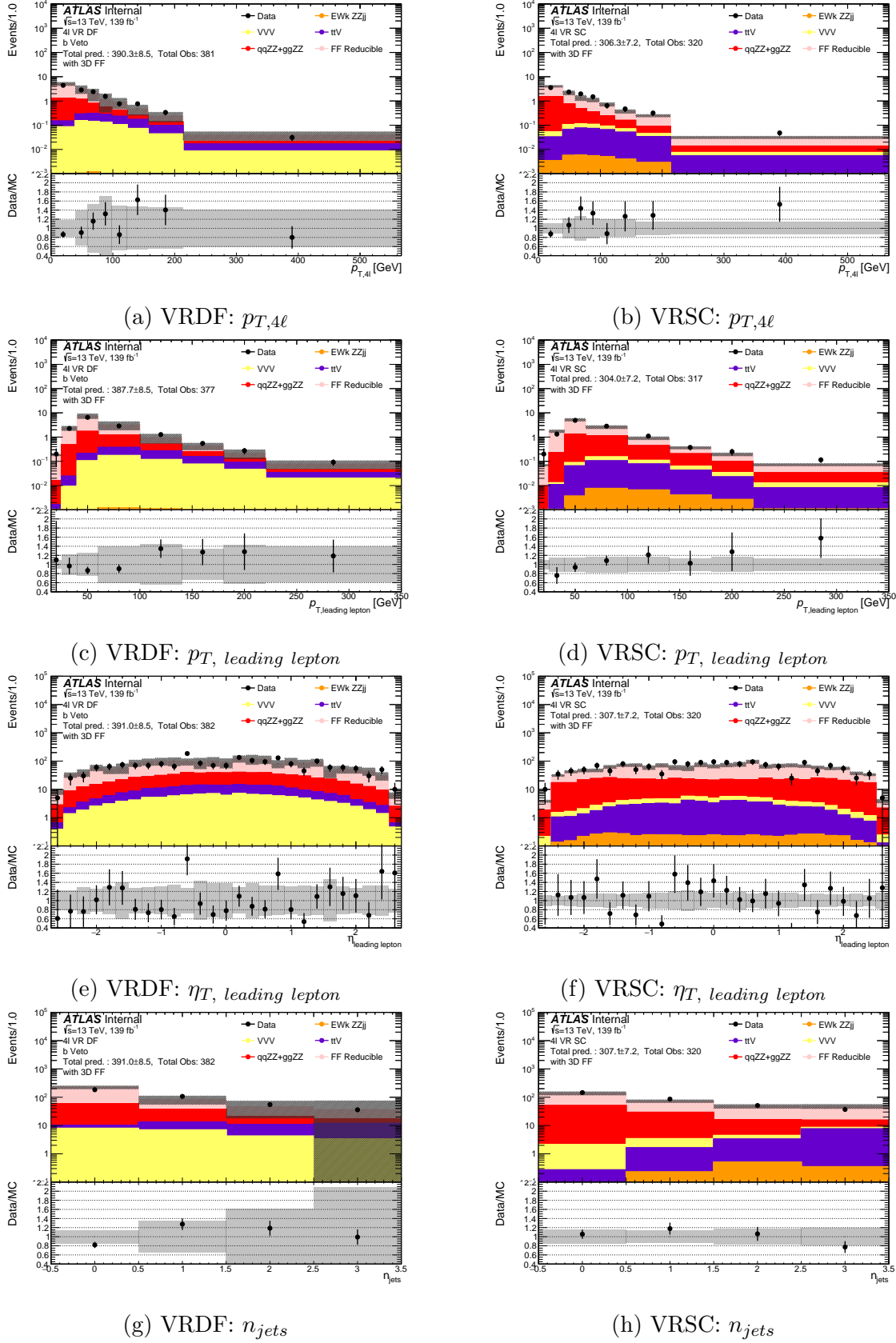


Figure 34: Data and MC yield comparison for different flavor validation regions (left) and same charge validation region (right) as a function of several kinematic observables. **remake**
plots with ATLAS Label and cleaning other **71**abs

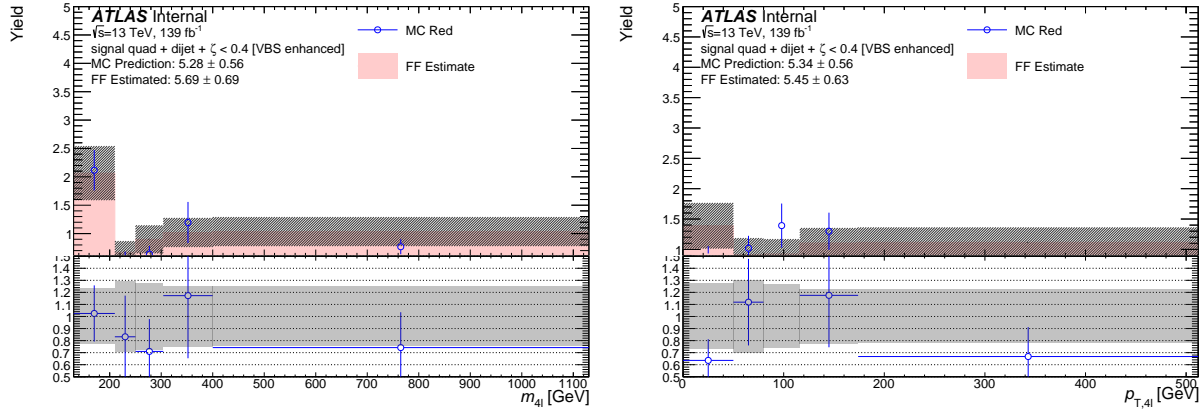


Figure 35: MC prediction and fake-factor method estimate of the fake background as a function of $m_{4\ell}$ (left) and $p_{T,4\ell}$ (right) in the VBS-Enhanced region. Black bands represent the systematic uncertainties from the fake factor method. [remake plots with ATLAS Label and cleaning other labels](#)

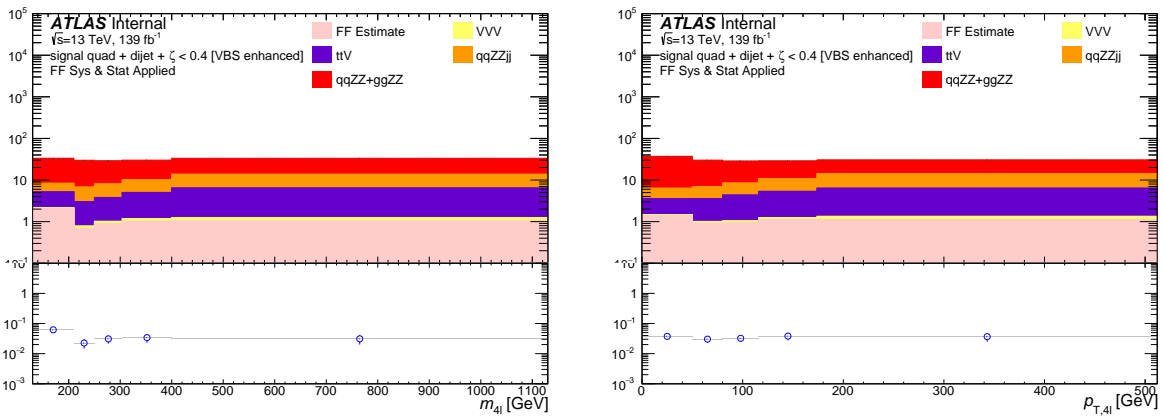


Figure 36: SM prediction and fake background estimated from the fake-factor method as a function of $m_{4\ell}$ (left) and $p_{T,4\ell}$ (right) in the VBS-Enhanced region. Black bands represent the systematic uncertainties from the fake factor method, which are negligible on the full signal region distribution. [remake plots with ATLAS Label, cleaning other label and y-axis/ratio-axis title](#)

14 Unfolding

The main results of the thesis are differential cross-section measurements at the particle level. The inclusive detector level cross-section for a given physics process $p_1 p_2 \rightarrow X$ is,

$$\sigma_{p_1 p_2 \rightarrow X}^{\text{detector level}} = A \times \epsilon \times \sigma_{p_1 p_2 \rightarrow X}^{\text{particle-level}} \quad (14.1)$$

where $\sigma_{p_1 p_2 \rightarrow X}^{\text{particle-level}}$ is the *true* cross-section of the physics process predicted by the theory.

The physical layout of the ATLAS detector does not cover all areas of the phase space. A accounts for the limited acceptance of the ATLAS detector. Several parts of the detector have several reconstruction efficiencies, which are accounted for by the factor ϵ . The detector level cross-section is measured experimentally in terms of the number of particles in a given final state (N) and integrated Luminosity L as $\sigma_{p_1 p_2 \rightarrow X}^{\text{detector level}} = \frac{N}{L}$. The *true* particle level inclusive cross-section can be estimated by correcting for detector acceptance and detector efficiency for the measured cross-section $\sigma_{p_1 p_2 \rightarrow X}^{\text{detector level}}$.

For differential cross-sections where the cross-section is measured in different bins of the kinematic observables, additional correction is needed to correct the resolution-induced migration between nearby bins.

This Chapter discusses the unfolding technique in detail. Section 14.1 gives an Overview on the unfolding algorithm, whereas Section 14.3 validates the unfolding method. Section 14.4 discusses the bias from unfolding and the attempts to optimize the bias.

14.1 Method Overview

The analysis uses an *iterative Bayesian unfolding* algorithm based on Baye's theorem [30]. Bayes' theorem formulates a mathematical relation to obtain a probability of an effect E caused by several independent causes C_i , given the initial probability of the causes $P(C_i)$ and the conditional probability of the $i - th$ cause to produce the effect $P(E|C_i)$ as,

$$P(C_i|E) = \frac{P(E|C_i).P(C_i)}{\sum_j P(E|C_j).P(C_j)} \quad (14.2)$$

The obtained probability depends on the prior probability of the cause and the conditional probability of cause and effect. The prior dependency is reduced by using an iterative technique, where the outcome of the previous iteration is used as a prior for the subsequent iteration.

For a single iteration, the algorithm can be summarized as,

$$U_i = \frac{1}{\epsilon_i} \times \sum_j^{reco\ bins} (R_j - F_j).f_i \cdot \frac{M_{ji}T_i}{\sum_k^{truth\ bins} M_{jk}T_k} \quad (14.3)$$

where U_i is the unfolded yield in the target bin i , T_i is the predicted truth level yield in particle bin i , R_j is the observed detector level yield in reco bin j and F_j is the subtracted detector level reducible background yield. M_{ij} is the migration matrix element from particle level bin j to detector level bin i .

Based on the discussion, conceptually, three corrections from the SM MC prediction need to be applied to estimate the unfolded yield. The three unfolding inputs are

- ***Reconstruction efficiency (ϵ):*** The reconstruction efficiency accounts for the limited acceptance and efficiency of the detector. Technically, it is defined as a fraction of events that pass both detector and fiducial level selection to the events passing only the fiducial level selection.
- ***Fiducial fraction (f):*** The fiducial fraction accounts for events that are outside the fiducial region at the particle level, which due to limited detector resolution entered in the measured distribution. An example of such an event would be a signal $4\ell + jj$ event where one of the jets originates from pile-up instead of hard-scatter. Technically, it is defined as a fraction of events that pass both detector and fiducial level selection to the events passing only the detector level selection.

- **Migration matrix** (M_{ij}): The migration matrix is a two-dimensional matrix that accounts for events migrated from particle level bin j to detector level bin i . The migration matrix corrects the probability of bin migration. It is measured in MC by comparing particle and detector levels distributions for events that pass both fiducial and detector-level selections. Bin migrations result from resolution effects and smearing of the reconstructed distributions. The diagonal component of the migration matrix is related to the *fiducial purity*, which corresponds to the fraction of detector-level events that originate from the same bin at the particle level.

Figure 37 show all three unfolding inputs along with the purity as a function of m_{jj} . The reconstruction efficiency is less than 50% caused by the poor jet reconstruction efficiency. The fiducial fraction and purity is smaller in lower bins of m_{jj} , which mainly corresponds to contribution from pileup jets faking the event selection. The normalized migration matrix shown in the second plot with the particle level prediction in $y - axis$ and the detector level prediction in $x - axis$ is diagonal.

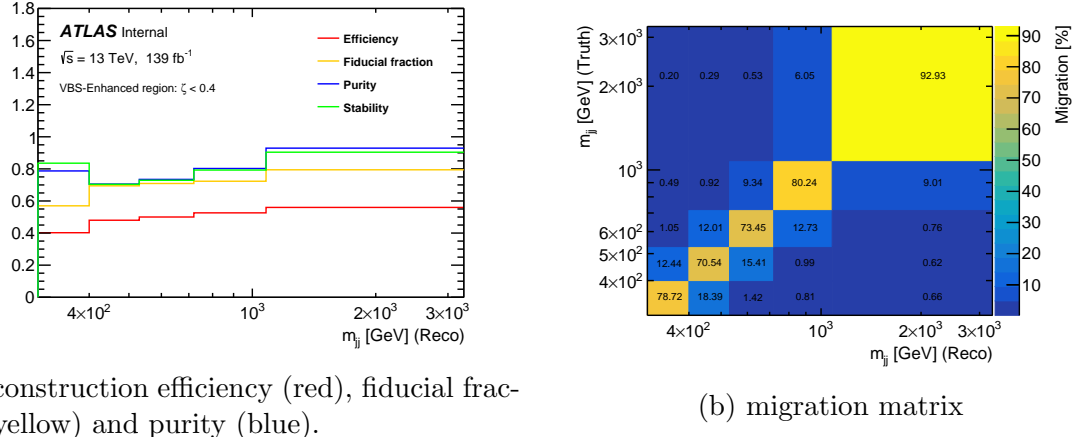


Figure 37: Unfolding inputs from SM MC as a function of m_{jj} . remake first plot with ATLAS Label and stability

14.2 Binning for Unfolding

Choosing optimal binning to perform the unfolding procedure for all kinematic observables effectively is imperative. Two factors drive the choice of binning; first, the necessity to have large enough bin statistics to maintain the Gaussian approximation while preserving the shape of the differential distributions, and second, the necessity to minimize large bin migrations and statistical uncertainties from unfolding. Therefore, each bin must have at least 15 events in the VBS-Suppressed region and at least 20 events in the VBS-Enhanced signal region.

To maintain a good performance of the unfolding, each bin for the kinematic observable has at least 70% purity except for $p_{T,4\ell jj}$ where at least 50% purity is required. Moreover, for each observable, every bin width must be equal to or greater than the resolution of the same bin. The resolution in each particle-level bin is evaluated from MC by comparing the difference of particle and detector level yield for events that pass both fiducial- and detector-level event selection. The difference is fitted using Gaussian approximation, and twice the resulting standard deviation is taken as the resolution. Table 12 shows the final bin choices for all the kinematic observables used in differential cross-section measurement. .

14.3 Method Validation

The unfolding method is validated using three different tests.

14.3.1 MC Closure Test

The first validation of the unfolding technique is with the SM MC. An SM-predicted detector level distribution for a kinematic observable is unfolded using the unfolding inputs from the same MC. Figure 38 shows an example of the MC-based closure test for m_{jj} in the VBS-Enhanced region. The blue detector-level MC prediction is unfolded using the inputs from the same MC, and the resulting black unfolded distribution is compared with the red particle-

Table 12: Binning for all unfolded observables in VBS-Enhanced and suppressed regions.

Observable	Region	Binning
m_{jj} [GeV]	VBS-Enhanced VBS-Suppressed	[300, 400, 530, 720, 1080, 3280] [300, 410, 600, 178]
$m_{4\ell}$ [GeV]	VBS-Enhanced VBS-Suppressed	[130, 210, 250, 304, 400, 1130] [130, 226, 304, 752]
$p_{T,4\ell}$ [GeV]	VBS-Enhanced VBS-Suppressed	[0, 50, 80, 116, 174, 512] [0, 76, 140, 424]
$p_{T,jj}$ [GeV]	VBS-Enhanced VBS-Suppressed	[0, 52, 82, 116, 172, 524] [0, 80, 146, 448]
$p_{T,4\ell jj}$ [GeV]	VBS-Enhanced VBS-Suppressed	[0, 20, 42, 64, 298] [0, 36, 70, 254]
$s_{T,4\ell jj}$ [GeV]	VBS-Enhanced VBS-Suppressed	[70, 240, 320, 420, 580, 1410] [70, 330, 500, 1210]
$ \Delta y_{jj} $	VBS-Enhanced VBS-Suppressed	[2, 3.08, 3.74, 4.32, 5.06, 7.4] [2, 2.94, 3.78, 5.4]
$\Delta\phi_{jj}^{signed}$	VBS-Enhanced VBS-Suppressed	$[-\pi, -2.1, 0, 2.1, \pi]$ $[-\pi, 0, \pi]$
$\cos\theta_{\ell i \ell j}^*$	VBS-Enhanced VBS-Suppressed	[-1, -0.5, 0, 0.5, 1] [-1, 0, 1]
ζ	VBS-Enhanced VBS-Suppressed	[0, 0.06, 0.12, 0.18, 0.26, 0.4] [0.4, 0.5, 0.64, 1.02]

level prediction. Since both detector-level prediction and unfolding inputs are from the same MC, a perfect closure between the unfolded and particle-level distribution is observed.

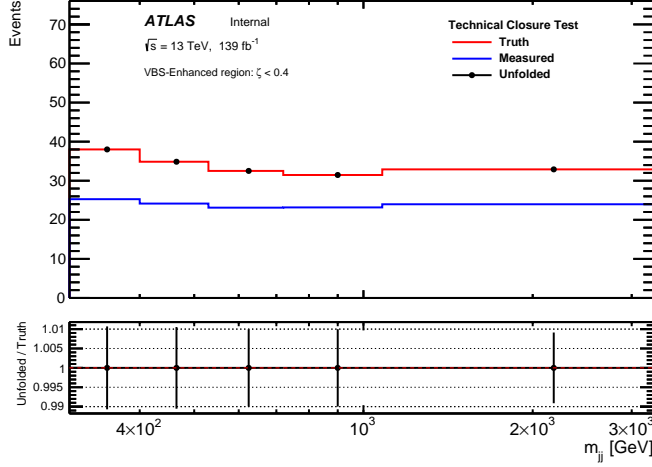


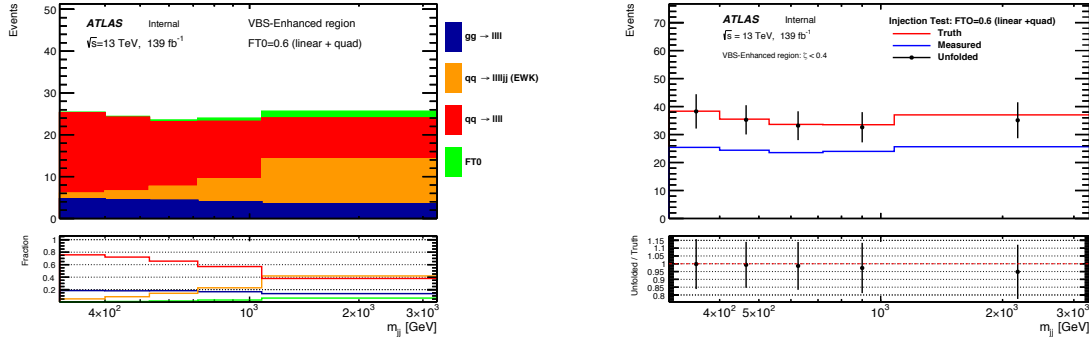
Figure 38: MC technical closure test of the unfolding procedure for m_{jj} . The detector-level MC distribution (in blue) is unfolded with the nominal SM unfolding inputs and compared to the particle-level distribution (in red) from the same MC. A perfect closure between unfolded and particle level distribution is observed

14.3.2 Injection Test

The analysis uses a model-independent EFT approach discussed in Section 17 to constrain the effect of BSM physics. Therefore, it is essential to test the ability of the unfolding algorithm to uncover the accurate particle-level prediction from data containing BSM physics via injection test. In an injection test, a BSM physics contribution is added to the SM detector-level prediction, unfolded with the nominal SM unfolding inputs, and compared with the BSM-added particle-level distribution. Figure 39a shows an injection test for m_{jj} in the VBS-Enhanced region where a BSM contribution (green distribution) is added to the SM MC. The BSM contribution is from linear and quadratic contributions of an *FT0* EFT operator. Figure 39b shows the result of the injection test. The BSM-added detector-level MC prediction (blue) is unfolded (black) using nominal SM MC unfolding inputs and compared against the BSM-added particle-level distribution (red). A small non-closure of

about 5% in the last bin of m_{jj} is observed, which is well within the uncertainties of the unfolded distribution.

Note to self: perhaps it makes sense to discuss EFT theory motivation in theory section?

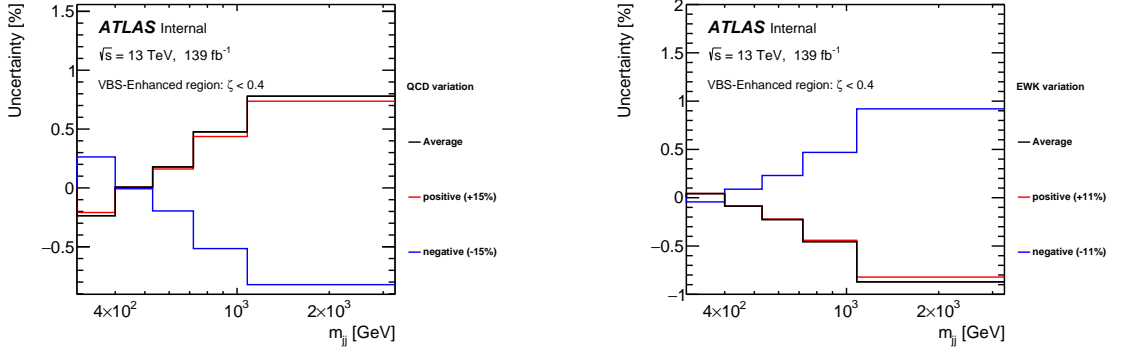


(a) Detector level MC prediction with contribution from dimension-8 $FT0$ EFT operator. (b) Unfolded SM+EFT MC detector-level distribution with response matrix from SM MC.

Figure 39: Injection test with dimension-8 $FT0$ EFT operator. remake plots with ATLAS Label

14.3.3 Physics Variation

From the previous ATLAS electroweak $ZZjj$ analysis, a slight enhancement on the central value of the EWk $ZZjj$ cross-section was measured [5]. The final unfolding validation tested the ability of the algorithm to recover the actual shape of particle-level distribution if a physics process cross-section was different from the SM prediction. First, as shown by figure 40a, the cross-section for parton-initiated QCD $qqZZjj$ is varied by a factor equal to the total statistical uncertainty on data in the VBS-Suppressed region $\pm 15\%$. The varied detector-level distribution is then unfolded using the nominal SM MC unfolding inputs and compared with the varied fiducial level prediction. Figure 40b shows the same test where the $EWKqqZZjj$ cross-section is varied by $\pm 11\%$ based on the enhanced cross-section observed in the previous measurement. In both cases, a non-closure of about 1% is observed, well below the uncertainties from unfolding.



(a) QCD cross-section is varied by $\pm 15\%$ (b) EWK cross-section is varied by $\pm 11\%$

Figure 40: Unfolding validation using physics variation where parton-initiated QCD (left) or the EWK process cross-sections are varied.

14.4 Bias and Optimization

The unfolded procedure relies on a prior value depending on the SM MC which naturally biases the unfolded cross-sections. With each iteration of unfolding, the algorithm improves the knowledge of the prior, thus, reducing the unfolding bias. However, with increasing number of iterations, the repeated bin migrations amplifies the statistical fluctuations in data, resulting in larger values of statistical uncertainties. Therefore, a finite number of iteration is chosen and the resulting unfolding bias is taken as the systematic uncertainty for the measurement.

The unfolding bias is evaluated by the *data-driven closure test*, where a pseudo dataset is developed utilizing the ratio of observed data and SM-predicted detector-level yield. First, for each observable the data and MC ratio is smoothed using Friedman’s Super Smoother technique [], fixing the end points to the value of ratio in the first and last bins. A reweighing function for each observable is developed to reweigh the SM fiducial- and detector-level yields. The reweighed detector-level signal-yield is then unfolded with the nominal unfolding inputs from SM and compared with the reweighed fiducial-level yield to get the final unfolding bias. Figure 41 shows step-by-step procedure for the data-driven closure test. As shown by the ratio panel of figure 41d, unfolding bias of order 10% is observed.

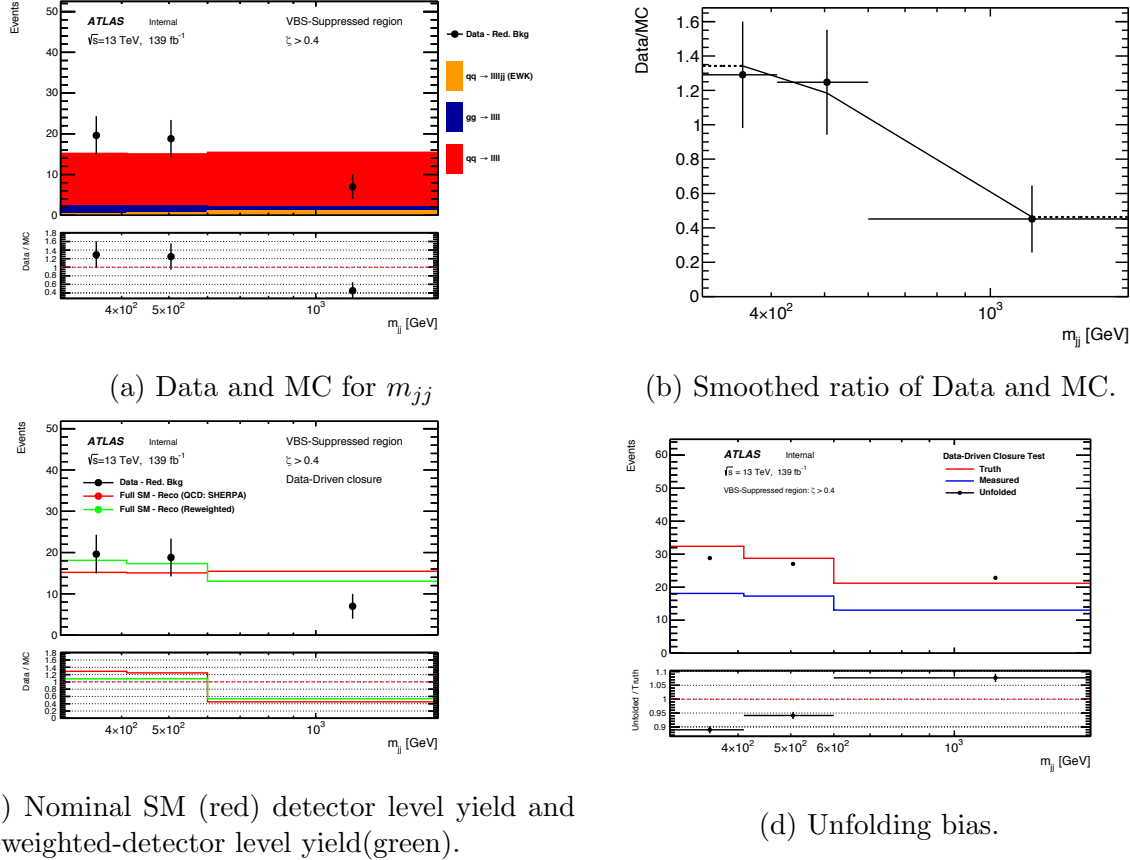


Figure 41: A step-by-step overview of the data driven closure test to get the unfolding bias. remake plots with ATLAS Label

The bias observed in figure 41d is obtained by using one number of iteration for unfolding. With a goal to reduce the unfolding bias, the data-driven closure test was repeated for several number of iterations. The resulting unfolding bias and systematic uncertainties up to 4 iterations are shown in figure 42. As expected the unfolding bias decreases whereas the statistical uncertainty increases with the higher number of iteration. To balance between the statistical uncertainty and bias uncertainty, one number of iteration is chosen as optimal choice for the measurement.

Unfolding bias is the largest source of the systematic uncertainty of the analysis and is studied in detail using a MC-driven toy studies to understand the source. The observed large bias is from detector-level pileup jets at lower p_T or higher η that are not part of the fiducial phase space. The jet-vertex-tagger and forward-jet-vertex-tagger has lower efficiency to select

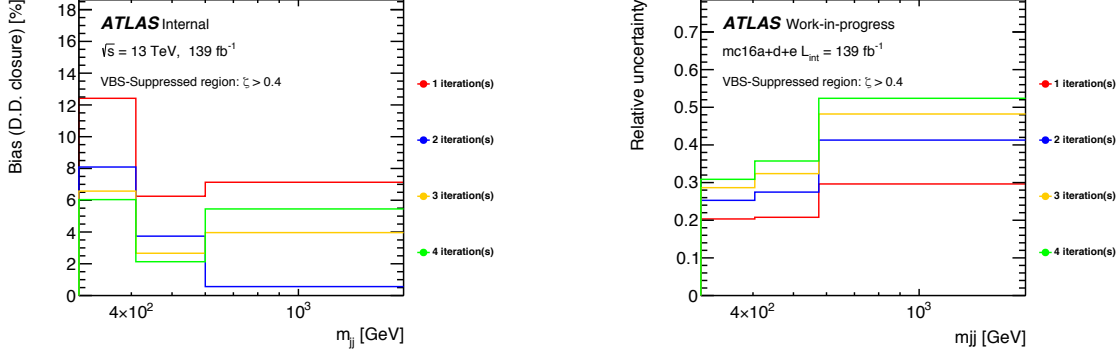


Figure 42: Unfolding bias (left) and statistical uncertainty (right) with up to 4 unfolding iterations as a function of m_{jj} in VBS-Suppressed region.

the hard scattering jets at lower p_T or higher η , thus resulting in more *fiducial-fake-event* contamination. The additional MC-based studies on the unfolding bias are summarized in Appendix B.

15 Uncertainties on the Measurement

15.1 Theoretical Uncertainties

15.2 Experimental Uncertainties

Chapter VI: Results

16 Differential Cross-sections

17 Effective Field Theory ReInterpretation

Chapter VII: Conclusion

Chapter VIII: Outlook

18 Run-3

19 High Luminosity LHC

References

- [1] P.A. Zyla et al. Review of Particle Physics. *PTEP*, 2020(8):083C01, 2020.
- [2] Francis Halzen and Alan Martin. *Quarks & Leptons: An introductory course in modern particle physics*. John Wiley & Sons, New York, USA, 1984.
- [3] Wikipedia contributors. Standard Model of Elementary Particles. https://en.wikipedia.org/wiki/Standard_Model, 2019. [Online; accessed 05-November-2022].
- [4] A. D. Martin, W. J. Stirling, R. S. Thorne, and G. Watt. Parton distributions for the LHC. *Eur. Phys. J. C*, 63:189–285, 2009.
- [5] ATLAS Collaboration. Observation of electroweak production of two jets and a Z -boson pair, 2020.
- [6] Yanyan Gao and Andrei V. Gritsan and Zijin Guo and Kirill Melnikov and Markus Schulze and Nhan V. Tran. Spin determination of single-produced resonances at hadron colliders. *Physical Review D*, 81(7), apr 2010.
- [7] Mark Thomson. *Modern particle physics*. Cambridge University Press, New York, 2013.
- [8] E. Noether. Invariante variationsprobleme. *Nachrichten von der Gesellschaft der Wissenschaften zu Göttingen, Mathematisch-Physikalische Klasse*, 1918:235–257, 1918.
- [9] Bernabeu, Jose”, and Murillo, Jesús Carnicer and Michelini, Marisa and Perea, Carmen. *Fundamental Physics and Physics Education Research*, chapter Symmetries in the Standard Model, pages 3–16. Springer International Publishing, Cham, 2021.
- [10] Sheldon L. Glashow. Partial-symmetries of weak interactions. *Nuclear Physics*, 22(4):579–588, 1961.
- [11] C. N. Yang and R. L. Mills. Conservation of Isotopic Spin and Isotopic Gauge Invariance. *Phys. Rev.*, 96:191–195, Oct 1954.
- [12] Nguyen, K. The Higgs Mechanism, 2009.
- [13] M. E. Peskin , D. V. Schroeder. *An Introduction to Quantum Field Theory*. Westview PRESS, Colorado, USA, 1995.
- [14] Buchmüller, W. and Lüdeling, C. Field Theory and Standard Model, 2006.
- [15] CMS Collaboration. Observation of a new boson at a mass of 125 GeV with the CMS experiment at the LHC. *Physics Letters B*, 716(1):30–61, sep 2012.
- [16] The ATLAS Collaboration. Observation of a new particle in the search for the Standard Model Higgs boson with the ATLAS detector at the LHC. *Physics Letters B*, 716(1):1–29, 2012.

- [17] The CDF II Collaboration. High-precision measurement of the W boson mass with the CDF II detector. *Science*, 376(6589):170–176, 2022.
- [18] Richard Massey, Thomas Kitching, and Johan Richard. The dark matter of gravitational lensing. *Reports on Progress in Physics*, 73(8):086901, jul 2010.
- [19] Peter Skands. QCD for Collider Physics, 2011.
- [20] Sergey Alekhin, Kirill Melnikov, and Frank Petriello. Fixed target Drell-Yan data and NNLO QCD fits of parton distribution functions. *Phys. Rev. D*, 74:054033, Sep 2006.
- [21] Sergey et al. Alekhin. The PDF4LHC Working Group Interim Report, 2011.
- [22] Andy Buckley et al. General-purpose event generators for LHC physics. *Physics Reports*, 504(5):145–233, 2011.
- [23] The CMS Collaboration. Evidence for electroweak production of four charged leptons and two jets in proton-proton collisions at $s=13\text{TeV}$. *Physics Letters B*, 812:135992, 2021.
- [24] Jager, B., Karlberg, A. and Zanderighi, G. . Electroweak ZZjj production in the Standard Model and beyond in the POWHEG-BOX V2. *J. High Energ. Phys.*, 141, 2014.
- [25] A. Denner and T. Hahn. Radiative corrections to $W+W^- \rightarrow W+W^-$ in the electroweak standard model. *Nuclear Physics B*, 525(1-2):27–50, 1998.
- [26] Tao Han and David Krohn and Lian-Tao Wang and Wenhan Zhu. New physics signals in longitudinal gauge boson scattering at the LHC. *J. High Energ. Phys.*, 2010(3), mar 2010.
- [27] Eduardo da Silva Almeida and O. J. P. Éboli and M. C. Gonzalez–Garcia. Unitarity constraints on anomalous quartic couplings. *Physical Review D*, 101(11), jun 2020.
- [28] Jung Chang, Kingman Cheung, Chih-Ting Lu, and Tzu-Chiang Yuan. WW Scattering in the Era of Post Higgs Discovery. *Physical Review D*, 87(9), may 2013.
- [29] Khoze, V., Ryskin, M., Stirling, W. et al. A Z-monitor to calibrate Higgs production via vector boson fusion with rapidity gaps at the LHC. *Eur. Phys. J.*, C 26:429–440, 2003.
- [30] Giulio D’Agostini. A multidimensional unfolding method based on Bayes’ Theorem. Technical report, DESY, Hamburg, 1994.
- [31] ATLAS Collaboration. ATLAS b -jet identification performance and efficiency measurement with $t\bar{t}$ events in pp collisions at $\sqrt{s} = 13\text{TeV}$. 2019.
- [32] J. Maurer, J. Reichert, E. Varnes. Technical discussion of FakeBkgTools. 2018.

Appendices

A Personal Contribution

B Additional Study on Unfolding Bias